



# Developments Toward Diagnostic Breast Cancer Imaging Using Near-Infrared Optical Measurements and Fluorescent Contrast Agents<sup>1</sup>

Daniel J. Hawrysz and Eva M. Sevick-Muraca<sup>2</sup>

Department of Chemical Engineering, Texas A&M University, College Station, TX 77843-3122 and  
School of Chemical Engineering, Purdue University, West Lafayette, IN 47907-1283

## Abstract

The use of near-infrared (NIR) light to interrogate deep tissues has enormous potential for molecular-based imaging when coupled with NIR excitable dyes. More than a decade has now passed since the initial proposals for NIR optical tomography for breast cancer screening using time-dependent measurements of light propagation in the breast. Much accomplishment in the development of optical mammography has been demonstrated, most recently in the application of time-domain, frequency-domain, and continuous-wave measurements that depend on endogenous contrast owing to angiogenesis and increased hemoglobin absorbance for contrast. Although exciting and promising, the necessity of angiogenesis-mediated absorption contrast for diagnostic optical mammography minimizes the potential for using NIR techniques to assess sentinel lymph node staging, metastatic spread, and multifocality of breast disease, among other applications. In this review, we summarize the progress made in the development of optical mammography, and focus on the emerging work underway in the use of diagnostic contrast agents for the molecular-based, diagnostic imaging of breast. *Neoplasia* (2000) 2, 388–417.

**Keywords:** photon migration, optical imaging, tomography, breast cancer, fluorescent contrast.

## 1.0 Introduction

The development of near-infrared (NIR) biomedical optical tomography has been a substantive effort involving a number of laboratory groups and focusing on a number of different measurement approaches and inverse methods. One common thread among these efforts is the concerted development of optical tomography toward diagnostic breast imaging in patients with cancer. The rationale behind NIR optical mammography has been recently summarized in the review by Tromberg *et al.* [1]: herein we provide a comprehensive review of the technologies associated with NIR imaging. Briefly, NIR optical tomography takes advantage of a “therapeutic window” between 700 and 900 nm in which tissues exhibit low absorbance, but high scattering capacity. As a result, light in this wavelength regime can scatter

through several centimeters of tissues before being extinguished by absorption. Absorption occurs primarily from the tissue chromophores of oxy- and deoxyhemoglobin, fat, melanin, and water, whereas scattering is typically due to refractive index differences of extracellular and intracellular structures. Table 1 lists literature values of the isotropic scattering and absorption coefficients,  $\mu'_s$ , and  $\mu_a$ , which represent the reciprocal length that a photon will travel within breast or other tissues before being scattered or absorbed. The ability to detect diseased tissues with NIR light depends critically on the “optical contrast,” or the consistent differences between the absorption and scattering properties of normal and diseased tissue volumes.

In the following, we briefly introduce the measurement methods by which optical tomography is conducted, the mathematics that describe how tissue optical property changes influence the measurements made at the tissue surface, and finally how these surface measurements can be used to render an image of interior tissue optical properties. Those readers less interested in the mathematics of the problem may skip Sections 3.1 and 3.2 without compromising comprehension. We next highlight the optical mammography measurements conducted by our colleagues that point to the rationale for augmenting endogenous contrast using exogenous fluorescent agents. The physics of fluorescence-enhanced optical tomography is discussed and for those interested readers, we describe the mathematics that describe how fluorescent agents impart optical contrast and how their use can ease the difficulties of image reconstruction. Finally, we highlight our own work as well as the work of our colleagues relating to the development of fluorescence-

Abbreviations: NIR, near-infrared; CW, continuous wave; TDPM, time-domain photon migration; FDPM, frequency-domain photon migration; FWHM, full width at half maximum; MRI, magnetic resonance imaging; SNR, signal to noise ratio; ICG, indocyanine green; ICCD, intensified charge-coupled device; PDT, photodynamic therapy; HPPH, hexylpyropheophorbide; LDL, low-density lipoproteins

Address all correspondence to: Dr. Eva M. Sevick-Muraca, Department of Chemical Engineering, Texas A&M University, College Station, TX 77843-3122.

E-mail: sevick@che.tamu.edu

<sup>1</sup>This review was supported in part by National Institutes of Health (NIH) K04CA6874 and R01 CA 67176.

<sup>2</sup>This work is dedicated to our mentors, Professor Rakesh K. Jain on the occasion of his 50th birthday and to Professor Britton Chance, in celebration of his pioneering work on photon migration.

Received 25 August 2000; Accepted 10 October 2000.

Copyright © 2000 Nature America, Inc. All rights reserved 1522-8002/00/\$15.00

**Table 1.** Literature Values of Scattering and Absorption Coefficients of Various Tissues.

Tissue type	Absorption coefficient $\mu_a$ ( $\text{cm}^{-1}$ )	Scattering coefficient $\mu_s$ ( $\text{cm}^{-1}$ )	Isotropic scattering coefficient $\mu_s'$ ( $\text{cm}^{-1}$ )	Wavelength of light (nm)	Reference
Breast <i>in vivo</i> (normal and tumor premenopause)	0.02 normal		7 normal	810	Tromberg <i>et al.</i> [130]
Breast <i>in vivo</i> (normal and tumor, postmenopause)	0.07 tumor 0.03 normal		9 tumor 7.5 norm	810	Tromberg <i>et al.</i> [130]
Breast <i>in vivo</i>	0.06 tumor		8 tumor		
Breast <i>in vitro</i> (normal, cancerous)	0.02–0.05 0.01–0.5		7–14 5–15	800 600–1000	Heusmann <i>et al.</i> [131] Peters <i>et al.</i> [132]; Troy <i>et al.</i> [133]
Breast <i>in vivo</i> pre-menopausal	~0.068		~11.3	760	Suzuki <i>et al.</i> [134]
Breast <i>in vivo</i> postmenopausal	~0.028		~7.6	760	Suzuki <i>et al.</i> [134]
Breast <i>in vivo</i> (normal, premenopausal)	0.05–0.16		8–11	670–960	Tromberg <i>et al.</i> [1]
Breast <i>in vivo</i> (normal, postmenopausal)	0.01–0.09		6–7	670–960	Tromberg <i>et al.</i> [1]
Breast Tumor <i>in vivo</i> , postmenopausal	0.07–0.17			670–960	Tromberg <i>et al.</i> [1]
Lung <i>in vitro</i>	~8.4	~40		630	Cheong <i>et al.</i> [135]; Beek <i>et al.</i> [136]
Breast <i>in vitro</i>	0.2–1.8	~400		630	Cheong <i>et al.</i> [135]; Beek <i>et al.</i> [136]
Liver <i>in vitro</i>	~3.2	~40		630	Cheong <i>et al.</i> [135]; Beek <i>et al.</i> [136]
Bladder, brain, heart, muscle, skin ( <i>in vitro</i> )	0.2–1.8			630	Cheong <i>et al.</i> [135]; Beek <i>et al.</i> [136]
Abdomen (normal, tumor)	0.07 normal 0.19 tumor		9.3 normal 7.8 tumor	811	Fishkin <i>et al.</i> [137]
Arm <i>in vivo</i>	0.12–0.13 0.07–0.11		12–13 9.6–9.4	660 700	Doornbos <i>et al.</i> [2]

enhanced contrast agents and imaging approaches. By way of conclusion, the use of fluorescence, NIR imaging for diagnostic breast imaging is discussed. This review seeks to concisely describe the physics, mathematics, and chemistry behind the developments of NIR diagnostic imaging of the human breast and of contrast-enhanced optical tomography for molecular-based diagnoses.

## 2.0 Types of NIR Optical Tomography of Whole Tissues

Three common NIR methods have been developed for imaging deep interior tissue volumes from noninvasive surface measurements that differ in the time dependence of the source intensity. This section gives a brief overview of the following techniques useful for diagnostic imaging of human breast: continuous wave (CW), time-domain photon

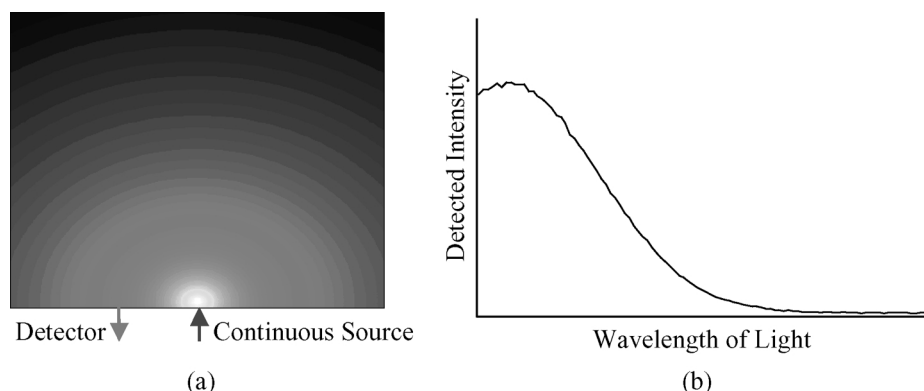


**Figure 1.** Schematic of continuous-wave measurement approach used in NIR optical imaging. (a) Continuous-wave (CW) imaging approaches utilize an incident, constant-intensity illumination that creates a steady light distribution in the tissue that exponentially attenuates with distance from a source point. (b) Measurement schemes can utilize the wavelength dependence of the attenuated light detected some distance away from the light.

migration (TDPM), and frequency-domain photon migration (FDPM) imaging.

### 2.1 Continuous-Wave (CW) Imaging

CW imaging measurements employ a light source whose intensity nominally does not vary with time. The constant intensity source is focused on the tissue surface and the tissue volume is illuminated with light whose intensity becomes exponentially attenuated with distance from the tissue surface (Figure 1). The time-invariant distribution of light intensity is subsequently detected at various positions on the tissue surface. The presence of diseased tissue regions may be characterized by wavelength-dependent light-absorption properties (i.e., tissue regions of varying vascular density) or light-scattering properties (i.e., tissue regions with larger and more numerous nuclei) than their surrounding normal tissues. In these tissue regions, propagating light is further attenuated when compared to the surrounding normal tissues. From the wavelength-dependent attenuation of light collected at the tissue surface, an interior map of the tissue optical properties is determined.

In highly scattering media such as tissues, photons can take one of many different paths *en route* from a source to a detector located at the air-tissue interface. Because the CW techniques have no means of detecting the distribution of the photon path lengths, they are limited in the amount of information they can provide for imaging of interior optical properties. In contrast to the time-dependent measurements that are described below, absolute values of optical properties of a uniform scattering medium cannot be determined from a single measurement made without careful and perhaps impractical calibration [2–4]. However, continuous-wave instrumentation is far simpler than that for time-dependent measurements, consisting only of a light source and a detector.

### 2.2 Time-Domain Photon Migration (TDPM) Imaging

Time-resolved methods involve launching an approximate impulse of light (of picoseconds or femtoseconds full width at half maximum [FWHM]) at the tissue surface and detecting the pulse that broadens and attenuates as it migrates through the tissue to another surface position located away from the source (Figure 2). The point-spread function, or the detected pulse, can be broadened to the order of 10 nsec during its migration through the tissue and to the detector on the tissue surface. The point-spread function also represents the distribution of “photon times-of-flight” spent migrating between the source and the detector, and is measured with picosecond or greater time resolution using photon-counting techniques or streak camera detectors. The measured distribution of photon times-of-flight and its various moments can be used to infer the optical properties of the tissue using a model-based optimization routine that assumes an incident Dirac delta impulse, or an impulse with an infinitely small FWHM. However, because most practical pulsed laser sources do not emit a Dirac delta impulse, the source function must be deconvolved from the point-spread function (or alternatively, the model must be convolved with

the point-spread function) for accurate recovery of the interior optical properties.

The required instrumentation associated with TDPM, namely a pulsed laser source, expensive and fast streak cameras or slow single-photon-counting detection systems, as well as the potentially lengthy times to acquire statistically significant numbers of photon counts, can all be significant drawbacks to the time-domain approach. Alternative to monitoring the distribution of photon times-of-flight, time-gating techniques can be applied in which the total number of photons that arrive at a detector within a prescribed time window are recorded (Figure 2f). Because scattering increases the times-of-flight spent by photons migrating in tissues, the photons that arrive earliest at the detector have encountered the fewest scattering events and are deviated least from the direct path between source and detector when compared to those photons with longer times-of-flight. Consequently, a spatial intensity image of early-arriving photons can conceivably be used to detect tissue regions of high absorbance (or high hemoglobin concentration) based on their attenuation. Yet the numbers of early-arriving photons and late-arriving photons can be statistically few in numbers, resulting in long measurement times (many repeated experiments) or statistical uncertainty in the measurements. Indeed, the large dynamic range of SNR over the entire distribution of photon times-of-flight in TDPM approaches can require significant data acquisition times to resolve or reduce uncertainty in the resulting images. However, some developers prefer to employ TDPM measurements to construct optical-property maps because its information content is the wealthiest [5].

### 2.3 Frequency-Domain Photon Migration (FDPM) Imaging

FDPM techniques are the focus of our imaging studies at the Photon Migration Laboratories at Texas A&M University (<http://www.chen.tamu.edu/pml>) as well as several other laboratories. In this technique, incident light intensity is sinusoidally modulated at a frequency on the order of 10 MHz to 1 GHz, with the most pertinent information in the 30- to 200-MHz range for the physiological range of optical properties. For those readers mathematically inclined, the modulated light source in the frequency-domain techniques is akin to a pulsed light source with a perfect Dirac delta function in the time domain. Hence, in the frequency-domain approaches, there is no need to convolve or deconvolve an instrument function with a model or from the actual measurements to accurately recover interior optical-property maps. In addition, laser diodes and LED light sources can be easily modulated given recent advances in oscillator technologies.

Once launched, the light intensity wave, or “photon density wave,” propagates through the tissue and becomes amplitude attenuated and phase-shifted relative to the source wave. The phase delay and amplitude attenuation of an intensity wave relative to the incident wave are detected at a point on the tissue surface located some distance away from its source (Figure 3). When

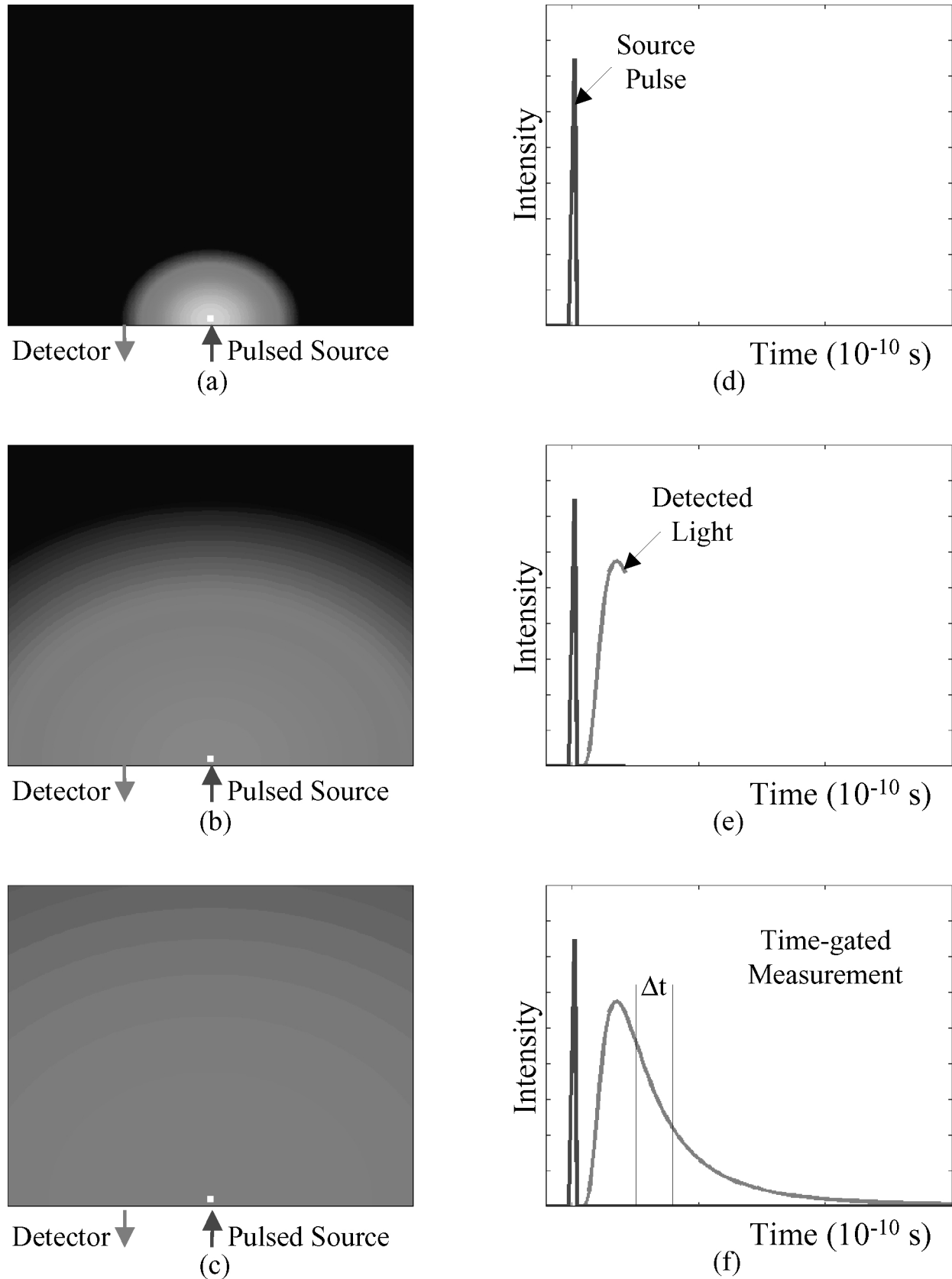


**Figure 2.** Schematic of time-domain measurement approaches used in NIR optical tomography. TDPM-imaging approaches utilize an incident impulse of light that results in the propagation of the pulse throughout the tissue that attenuates as a function of distance from the source and time following its incident impulse. The detected pulse is measured as intensity versus time and represents the photon times-of-flight. Panel (a) illustrates the light distribution in tissue from a pulse point source after  $1 \times 10^{-10}$  second, (b)  $25 \times 10^{-10}$  second and (c)  $150 \times 10^{-10}$  second following the incident impulse. The corresponding recorded data during the time intervals at the detector is illustrated in panels (d) through (f). A time-gated illumination measurement is shown in panel (f) in which the integrated intensity measured within a specified window is measured.



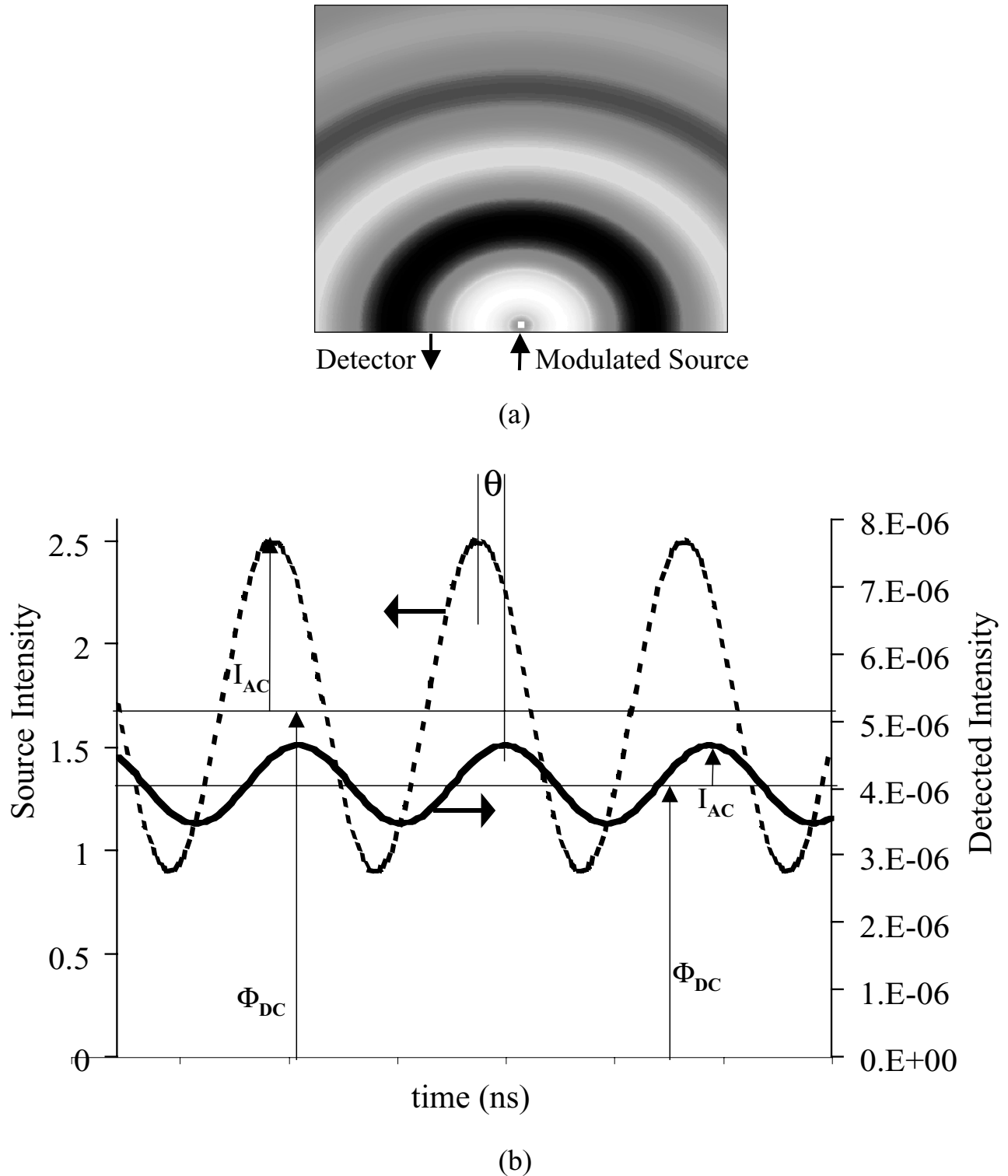


**Figure 3.** Schematic of the frequency-domain measurement approach used in NIR optical tomography. FDPM imaging consists of an incident, intensity-modulated light source that creates a “photon density wave” that propagates continuously throughout the tissue. Panel (a) is a depiction of light distribution in tissue due to a modulated source (exaggerated for purposes of illustration) and panel (b) illustrates the detected signal (in red) in response to the source illumination (in blue). The typical frequency-domain data, where the measurable quantities are the phase shift, the amplitude of each wave  $I_{AC}$ , and the bias of each wave  $\Phi_{DC}$ . As shown in panel (b), the intensity wave that is detected some distance away from the source is amplitude attenuated and phase-delayed relative to the source.

the photon density waves encounter tissue regions of varying optical properties, they refract, scatter, and interfere, as any other wave [6–9]. Hence these waves, when incident on a light-absorbing heterogeneity within a

tissue, can “reflect” and add to the propagating photon density wave as well as to other “reflected” waves. The result is a perturbation in the measured phase delay and amplitude attenuation whose magnitude is dependent on



the location, size and optical contrast of “heterogeneities” within a tissue volume. Using model-based approaches briefly described below, measurements of phase delay and amplitude attenuation are then used to reconstruct an interior optical-property map. It is noteworthy that, when properly designed, FDPM measurements can be self-calibrating and do not require an external calibration standard for referencing [10]. This is due to the fact that FDPM (as well as TDPM) measures the time-dependent migration characteristics of detected light rather than the intensity or amount of light detected [11].

### 3.0 Models to Predict Light Propagation and Their Use in Tissue Imaging

Conventional medical and microscopic imaging modalities depend on measurement of a signal, whether it be light, radiofrequency, X-ray, positrons, gamma radiation, etc., whose source can be directly attributed to a single volume element, or a linear path in the case of X-ray computed tomography, within the tissue or sample. Consequently, the image reconstruction in three dimensions is comparatively straightforward and involves relating the detected signal to the responsible tissue volume element. NIR optical tomography works differently. Whether CW, TDPM or FDPM measurements are involved, the signals acquired are NOT associated with a single tissue volume element, but rather the weighted sum of the entire tissue volume (Figure 4). The weighting factor for each volume element

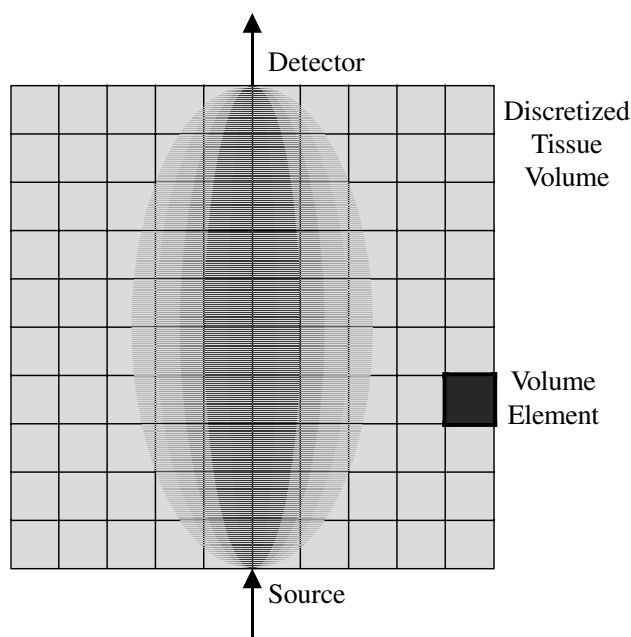
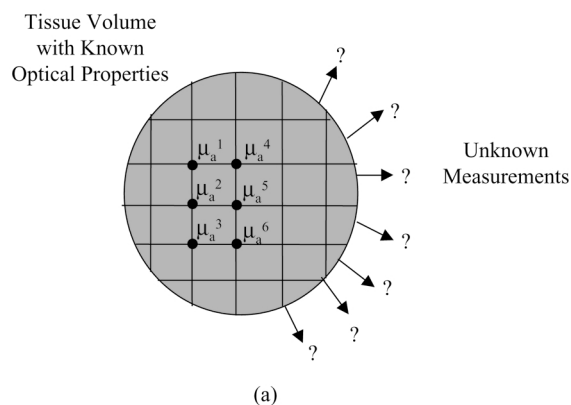


**Figure 4.** The differences between NIR optical tomography and other conventional imaging modalities is illustrated herein. In conventional imaging modality, the signal used to reconstruct an image originates from one volume element, or voxel, from the tissue while in NIR optical tomography techniques, the measured signal has weighted contributions from a number of different volume elements through which propagating light can travel from the source to the detector on the tissue surfaces.

### The Forward Imaging Problem:



### The Inverse Imaging Problem:

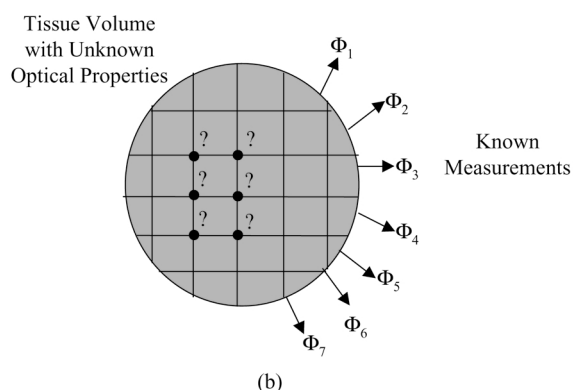


**Figure 5.** General illustration of (a) the forward imaging problem in which the tissue optical properties are known and used to predict the measurement and (b) the inverse imaging problem in which the measurements are used to obtain the unknown tissue optical properties.

is determined by the probability that the migrating light will actually propagate to and “sample” that tissue volume element. The probabilities can be computed from the model of light propagation.

To understand how NIR optical tomography is accomplished, one must recognize that two problems are involved. The FORWARD imaging problem consists of using a model to predict light propagation and the resulting measurements at the tissue–air interface given the spatial distribution of tissue optical properties within the entire volume. The INVERSE imaging problem then uses measurements at the tissue–air interface to determine the spatial distribution of the tissue optical properties (Figure 5). In the next two sections, we briefly highlight the mathematics for the FORWARD and INVERSE solutions for completeness. For those readers less interested in the computational aspects of the optical tomography problem, they can continue directly to Section 3.3 without loss of clarity.

#### 3.1 Solution to the Forward Imaging Problem

Regardless of the measurement approach employed, one can approach the modeling of light propagation through tissue by either a microscopic or a continuum approach [12]. The microscopic approach uses the Maxwell equations and is the more exact and fundamental method, but the tissue must be characterized exactly on the microscopic level and

the benefits to using this method are quickly lost in the burden of computation. Alternatively, the continuum approach describes the propagation of light with transport theory, which is akin to the accounting of photons, or a description of the transport of photon energy through the medium [13,14]. Transport theory as applied to photon migration has also been shown to agree with experimental measurements in tissue [15]. For the case in which scatter predominates over absorption, the diffusion approximation to the radiative transport equation can be utilized to more simply model light propagation in tissues (for example, see Ref. [16]).

**3.1.1 Models for CW and TDPM light propagation** Once the diffusion approximation is incorporated into the radiative transfer equation, a photon diffusion equation may be written to predict CW and TDPM measurements:

$$\nabla \cdot (D \nabla \Phi(\vec{r}, t)) - \mu_a \Phi(\vec{r}, t) = \frac{1}{c} \frac{\partial \Phi(\vec{r}, t)}{\partial t} - S(\vec{r}, t) \quad (1)$$

where  $D$  is the optical diffusion coefficient (cm) given by:

$$D = \frac{1}{3[\mu_a + \mu'_s]} \quad (2)$$

The fluence,  $\Phi(\vec{r}, t)$  ( $\text{W}/\text{m}^2$ ), is the angle-integrated, scalar flux of photons and is defined as the power incident on an infinitesimally small sphere divided by its area. Alternatively, it can also be thought of as the local concentration of photons times the speed of light at a given position  $\vec{r}$  and time  $t$ . For continuous-wave imaging, there is no time dependence and the source term,  $S(\vec{r}, t)$  becomes time invariant. Assuming it is an isotropic source, it is equal to the power deposited over its area. For TDPM measurements, the source,  $S(\vec{r}, 0)$  is assumed to be a Dirac delta function assuming a finite value at time zero, but zero at all other times. For both CW and TDPM measurements, Equation 1 can be solved to predict the fluence,  $\Phi(\vec{r})$  or  $\Phi(\vec{r}, t)$ , in response to the known spatial distribution of absorption and scattering properties of the tissue volume,  $\mu_a(\vec{r})$  and  $\mu'_s(\vec{r})$ .

Because a closed-form solution exists only for simple geometries, the solutions are developed numerically, using finite difference or finite element methods (see Section 3.1.3 below). Of the three boundary conditions commonly used for biologic applications of the diffusion equation, the partial current condition is the most rigorous [17,18]. It states that a photon leaving the tissue never returns, and uses a reflectance parameter to account for Fresnel reflection at the tissue–air surface. A slightly simpler condition, the extrapolated boundary condition, is an approximation of the partial current condition and yields similar solutions to the diffusion equation [15,19]. The third boundary condition, the zero condition, merely sets the fluence to zero on the boundary and is used for its simplicity. In a homogeneous scattering medium, the zero-boundary condition results in an analytic solution to the diffusion equation in terms of the absorption and scattering coefficients [19,20].

The measured flux or photon current in CW or TDPM measurements,  $J(\vec{r})$  or  $J(\vec{r}, t)$ , is then determined by the gradient of fluence at the surface:

$$J(\vec{r}, t) = -D \nabla \Phi(\vec{r}, t) \quad (3)$$

**3.1.2 Model for FDPM light propagation** FDPM measurements also employ the diffusion equation for solution of the forward solution, with the difference that the equation is cast in the frequency domain, rather than in the time domain:

$$\nabla \cdot (D \nabla \Phi(\vec{r}, \omega)) - \left[ \mu_a + \frac{i\omega}{c} \right] \Phi(\vec{r}, \omega) + S(\vec{r}, \omega) = 0 \quad (4)$$

Here the fluence,  $\Phi(\vec{r}, \omega)$ , is now a complex number describing the characteristics of the photon density wave at position  $\vec{r}$  and modulated at angular frequency  $\omega$ . Moreover, the fluence is comprised of alternating,  $\Phi_{AC}(\vec{r}, \omega)$  and nonalternating,  $\Phi_{DC}(\vec{r}, \omega)$  components of which the former can provide an accurate description of the phase delay and amplitude of the wave at position  $\vec{r}$ :

$$\Phi(\vec{r}, \omega) = \Phi_{AC}(\vec{r}, \omega) + \Phi_{DC}(\vec{r}, 0) = I_{AC} \exp(i\theta) + \Phi_{DC}(\vec{r}, 0) \quad (5)$$

The nonalternating component of the fluence,  $\Phi_{DC}(\vec{r}, 0)$  is simply the fluence that is measured when using a continuous-wave source. The pre-exponential factor,  $I_{AC}$ , is the amplitude of the photon density wave and the exponential factor,  $\theta$ , is the phase delay of the wave relative to the incident source. At larger modulation frequencies, the photon density wave attenuates more rapidly during its propagation and experiences greater phase lag. Consequently, the amplitude decreases with increasing modulation frequency whereas the phase delay increases with modulation frequency. Often the amplitude or modulation ratio is reported as a measurement. The modulation ratio is simply the amplitude of the wave normalized by  $\Phi_{DC}(r, 0)$ .

The frequency-domain diffusion equation is an elliptic differential equation that is typically solved numerically by a finite difference scheme or the Galerkin finite element method using one of the three boundary conditions listed above. Typically, finite difference methods are confined to rectangular geometries whereas finite element is more flexible to include partial current boundary conditions and can be adapted to the frustum or other geometries that are pertinent for noncompressive, diagnostic breast imaging [21]. However, it is important to remember that these numerical approaches provide approximate solutions of the diffusion equation, which in itself is an approximation.

**3.1.3 Diffusion model accuracy and numerical solution techniques** The accuracy of the diffusion approximation described for each of the measurement approaches has been studied in a tissue-mimicking, multiply scattering media and has been compared to the numerical solution of the full radiative transport equation [22]. These studies show that the accuracy of the diffusion approximation suffers slightly near boundaries and sources. It estimates



fluence rates and fluxes well in an isotropically scattering environment but errors are noticeable when the anisotropy factor is greater than  $\sim 0.6$ , which is generally the case for tissues and other biologic media. The anisotropy factor,  $g$ , is defined as the average cosine of the scattering angle and varies from 0 for an isotropic medium to 1 for a forward scattering medium. The errors are particularly large for anisotropy factor greater than 0.85 when a continuous-wave source is used [23]. However, the errors due to the anisotropy of the tissue are negligible if the source–detector separation is greater than about 10 transport lengths [24]. A transport length is defined as  $(\mu_a + \mu'_s)^{-1}$  and is the mean length that a photon travels in a given direction. These limitations must be carefully considered when modeling measurements conducted on a tissue system with the diffusion approximation.

In addition, when utilizing numerical methods, inaccuracies owing to discretization must be considered. To gain adequate image resolution and reduce discretization error, the meshes in finite difference and finite element must be finely resolved. These fine meshes cause the dimensionality of the imaging problem to become very large, which consequentially results in a computationally intensive solution to the inverse imaging problem. To alleviate this difficulty, multigrid finite difference methods are used for the modeling of photon transport in the some of the work described herein [25–28]. The multigrid finite difference method solves the problem first on a coarse mesh and then on a finer mesh using the solution from the coarse mesh as an initial guess. In this fashion, the computational intensiveness associated with the forward solution is avoided while maintaining resolution and reducing discretization error [25,29,30].

Finite-element methods are more appropriate for physiological tissue shapes and can also impart computational efficiency in solution of the inverse problem when appropriately coded [31–33]. However, because these 3D geometries are not rectangular, they present significant challenges when adapting multigrid approaches or dual-meshing schemes that employ finely resolved meshes for the accurate solution of the forward problem and a coarser mesh for the inverse solution.

With a relatively accurate model of light propagation in tissues, the opportunity to use the diffusion model to invert CW, TDPM, or FDPM measurements is possible. Typically, a number of measurements are recorded at discrete points on the air–tissue interface as either a point source is scanned across the tissue surface, or a number of individually placed sources consecutively provide incident light at fixed positions. Generally, the number of individual measurements conducted is comprised of the number of sources or source point locations,  $s$ , times the number of detectors or detector point locations,  $d$ . A critical issue is the rapidity with which  $s \times d$  measurements can be accurately made within a clinically realistic time frame so that an image may be recovered on solving the inverse problem. In the following section, we review the approaches to solve the inverse imaging problem, i.e., to determine the spatial map of  $\mu_a$  and

$\mu'_s$  from measurements conducted on the tissue surface. In Section 3.3 we summarize the approaches used for conducting NIR tomography measurements on tissue volumes and present a few examples of the images recovered from the solution to the inverse imaging problem.

### 3.2 Solution of the Inverse Imaging Problem

As explained above in Section 3, measurements of multiply scattered NIR light at the tissue–air interface in themselves do not provide direct information about interior tissue optical properties. These measurements merely describe the amount of light or attenuation of intensity; the altered distribution of photon times-of-flight; or the wave perturbations from which the spatial interior “map” of optical properties can be inferred. To determine the optical properties that govern light propagation from CW, TDPM or FDPM measurements conducted at the tissue surface, an inverse problem must be solved.

Attempts to solve the optical tomography problem have been made both by solving a formal inverse problem and by taking a less rigorous model-based approach. The solution of a formal inverse problem requires the use of the appropriate mathematical models described in the section above. Specifically, a guess of the interior optical properties is iteratively updated until the predicted measurements given by the solution of the forward problem matches the actual measurements. Because the number of unknowns (or optical properties) is greater than the number of measurements, the problem is underdetermined and especially difficult. This inverse problem is unavoidably “ill-posed,” a term that generally means that the solutions are non-unique and unstable in the presence of measurement error. In addition, the optical tomography problem is highly nonlinear and attempts to linearize it result in solution instabilities and often intractably long computational times if the update step is to remain within the range of accuracy of the linearization. The solution of the inverse problem is an intensive area of research in itself that is motivated by the several different research areas, including biomedical NIR optical tomography. To assess the performance of an inverse problem algorithm, the achieved solution must be compared to the known distribution of optical properties. As a consequence, studies to investigate the inverse optical tomography problem are performed using either (1) “synthetic” measurements, i.e., measurements that are predicted by the forward problem to which artificial random “noise” is added to simulate measurement error; or (2) phantom studies in which tissue-mimicking scattering media of known optical properties are used to collect experimental CW, TDPM, or FDPM measurements, which are used for the inverse solution.

This section first describes the empirical approaches to solve the inverse imaging problem and then proceeds to survey some of the formal inverse problem formulations using a variety of synthetic and phantom study measurements. A survey of this recent work toward the solution of the inverse imaging problem is listed in Table 2. In Section 3.3 the measurement and inverse approaches used in actual tissue studies for breast imaging are presented.

**Table 2.** Survey of Literature Work Involving the Solution of the Inverse Imaging Problem.

Author	General inversion formulation	Data type	Noise considered?	2D or 3D	Forward method	Measurement mode
Cubeddu <i>et al.</i> [35]	Localization	Phantom	Yes	3D	None	TDPM
Boas <i>et al.</i> [36]	Localization	Simulated	No	3D	None	FDPM
Fantini <i>et al.</i> [34]	Localization	<i>In vivo</i>	Yes	3D	None	TDPM
Grosenick <i>et al.</i> [5]	Localization	<i>In vivo</i>	Yes	3D	None	TDPM
Graber <i>et al.</i> [42]	Backprojection	Phantom	Yes	2D	Monte Carlo	CW
Walker <i>et al.</i> [43]	Backprojection	Phantom	Yes	2D	None	FDPM
Colak <i>et al.</i> [40]	Backprojection	Phantom	Yes	2D, 3D	FD	CW
Matson and Liu [39]	Backprojection	Simulated	Yes	3D	MFD	FDPM
Colak <i>et al.</i> [64]	Backprojection	<i>In vivo</i>	Yes	3D	Analytic	CW
Gonatas <i>et al.</i> [47]	Integral (non-iterative)	Phantom	Yes	3D	Analytic	CW/TDPM
O'Leary <i>et al.</i> [46]	Integral (non-iterative)	Simulated	Yes	3D	NS	FDPM
Yao <i>et al.</i> [25]	Integral (BIM)	Simulated	Yes	2D	MFD	FDPM
Ye <i>et al.</i> [51]	Integral (DBIM)	Simulated	Yes	2D	FD	FDPM
Cheng and Boas [48]	Integral (Born)	Phantom	Yes	pseudo-3D	NS	CW
Pogue <i>et al.</i> [27]	Differential (Newton–Raphson)	Phantom/simulated	Yes	3D F/2D I	MFD	FDPM
Pogue <i>et al.</i> [138]	Differential (Newton–Raphson)	Simulated	No	3D F/2D I	MFD	FDPM
Jiang <i>et al.</i> [139]	Differential (Newton–Raphson)	Phantom/simulated	Yes	2D	FEM	FDPM
Schweiger and Arridge [140]	Differential (Conjugate Gradient)	Simulated	No	2D, 3D	FEM	TDPM
Hielscher <i>et al.</i> [54]	Differential (Gradient-based Optimization)	Simulated	Yes	3D	FD	TDPM
Arridge <i>et al.</i> [60]	Differential (Gradient-based Optimization)	Phantom/simulated	Yes	3D	FEW	TDPM
Schmidt <i>et al.</i> [59]	Differential (Conjugate Gradient)	Phantom	Yes	2D	FEM	TDPM
Gao <i>et al.</i> [141]	Differential (Newton–Raphson)	Simulated	No	2D	FEM	FDPM
Pogue <i>et al.</i> [53]	Differential (Newton–Raphson)	Phantom/simulated	Yes	2D	FEM	FDPM
McBride <i>et al.</i> [70]	Differential (Newton–Raphson)	<i>In vivo</i> /simulated	Yes	2D	FEM	FDPM

FD, finite difference; MFD, multigrid finite difference; FEM, finite element method; NS, not specified; F, forward problem; I, inverse problem.

**3.2.1 Localization** Perhaps the simplest method for tomography is the localization method. The location and size of a tumor is estimated by rough measurements of transillumination intensity or, in the case of FDPM, phase shift. Using this information, an analytic solution to the diffusion equation is selected to match approximately the geometry of the tissue. An optimization routine is then used to match the prediction of the analytic solution to the diffusion equation with the observed data by varying the optical properties of the tissue and inclusion. Localization is the only technique described herein that uses analytic models to solve the tomography problem. Although not a full inversion method, this technique has produced optical images of *in vivo* human tissues as will be described in Section 3.3. The localization method can be based on an analytic solution of the diffusion model for a homogeneous semi-infinite medium [5,34,35] or an infinite slab [36] containing a spherical tissue volume with differing optical properties.

In the latter case, the difference between the experimentally obtained data and the analytic model prediction is minimized with a nonlinear optimization routine (often the Levenberg–Marquardt routine) by varying the optical properties and the depth of the spherical tissue volume. To determine the optical properties of the tissue volume relative to the surrounding normal tissues, the position and size of the heterogeneous region must be known, which is one of the major disadvantages of the approach.

In the former case, using time-resolved data, time-gated transillumination measurements of unscattered or minimally

scattered light are used to estimate the position and size of the inclusion [37]. Using frequency-domain measurements, Fantini and coworkers [34] used values of the phase delay and amplitude attenuation measured between a point source and a point detector positioned across the tissue (transillumination geometry) and raster-scanned in tandem. From the measurements, they computed a number reflective of tissue absorption to identify a light-absorbing tissue volume from the 2D scans. In yet another approach employing the same measurement geometry, the point-spread function or photon times-of-flight between a source and detector was measured using TDPM techniques and fit to the analytical solution of the optical diffusion equation assuming the tissue is homogeneous. A map was derived from the effective optical properties computed from the measurements obtained during the scanning of the source–detector pair to identify tissue volumes with high absorbance associated with angiogenesis or high vascularity [5]. As with all inversion approaches, the diffusion approximation is suspect at edges and boundaries, creating artifacts if edge effects are not empirically accounted for. Advantages to the image reconstructions based on the localization methods are that they evade the full inverse problem and result in comparatively short computational times (often less than 5 minutes).

**3.2.2 Backprojection** A class of imaging methods that has been adapted from X-ray computed tomography and electrical impedance tomography for use in diffuse optical tomography is derived from the backprojection technique



[38]. In general, backprojection algorithms assign the attenuation of radiation between a source and detector along the straight line or a defined path that connects the pair. When this procedure is repeated for several source–detector orientations, an image results that maps tissue densities. Diffraction tomography similarly “backpropagates” a detected scattered wave to its source, again generating an image when repetitively performed for a number of source–detector pairs. In backpropagation techniques of multiply scattered NIR light, the diffusion equation describes the path between the source–detector pairs (for a recent review see Ref. [39]). Backprojection and propagation algorithms have the advantage that they avoid the full inversion problem and can produce images in a comparatively short amount of computer time. These techniques have been proposed or demonstrated for CW [40–42], TDPM and FDPM [39,43] approaches. As described below, clinical measurements using a CW system developed by Phillips effectively employs backprojection algorithms [44].

**3.2.3 Integral formulation** One of the more common methods of formulating the inverse problem is by way of an integral treatment. The tissue containing the diseased volume is assumed to have uniform optical properties (called the “background properties”) whose values are estimated from *a priori* information. The approach is based on the assumption that a small change in the optical properties of a small tissue volume element causes a perturbation in the measurement at the air–tissue interface. Because these perturbations are additive, these small changes sum or integrate to contribute to the actual signal measured at the air tissue interface. Hence for each measurement involving a single source and a single detector, an equation summing the weighted, small optical property changes in each tissue volume element must be solved. The weighting factors are derived using the solution to the appropriate optical diffusion equation assuming that the optical properties are otherwise uniform and equal to the background optical properties [45]. It should be noted that this is known as “Born approximation” and provides a rough estimate of the image [46–48]. The drawback to using the Born and Rytov approximations is that it may be difficult to detect more than one heterogeneous tissue volume [49]. This difficulty may be alleviated if the weighting factors are iteratively recalculated with the updated optical-property maps. Integral methods that iteratively update the weighing factors are termed the Born iterative method (BIM) or the distorted Born iterative method (DBIM) [50]. In the BIM, the weighting factors are only partially corrected, whereas in the DBIM they are fully corrected at the expense of additional computational time [25,51].

**3.2.4 Differential formulation** A second approach of the full inverse imaging problem is the differential formulation. Like the integral approach, an initial guess of the optical properties is needed and is then iteratively adjusted using measurement data. The general solution is as follows. The forward problem is first solved using the guess of the optical-

property map and a set of predicted measurements is computed. Because the assumed optical-property map is usually not correct, these predicted measurements do not exactly match the actual measurements. We term this approach the differential formulation because a small change in the predicted measurements is directly expressed in terms of a small change in the optical properties using a Jacobian matrix. (The Jacobian matrix specifies how the predicted measurements change with a differential change in the optical properties at each position within the tissue.) The Jacobian matrix is then used to update the estimates of the optical-property maps.

Like the integral approach, the differential inverse problem is cast as an optimization problem to minimize the difference between the true measurements and those predicted by the forward solution using the iteratively updated optical-property map. Consider a hypothetical case in which a homogeneous region of tissue contains a single inclusion or heterogeneity whose position and size are known, but whose absorption coefficient is unknown. The problem is then to minimize the difference between the measured and predicted data by adjusting the absorption coefficients of the heterogeneity and its surroundings (or the “background”). Figure 6 illustrates a simplistic 3D map of the error between predicted and acquired measurement as a function of these two parameters. This is a simplistic schematic because in imaging, the position and size of heterogeneities are unknown and the number of unknowns can range in the tens of thousands, rather than simply two. Nonetheless, the differential approach seeks to find the minimum error between predicted and measured values, or the valley, for a particular set of optical properties by using the slope of the surface to update the optical-property map. The slope is effectively the Jacobian defined above. The error between the measured and predicted measurements is called the “objective” function and at its minimum, the correct image reconstruction is found. As in any optimization problem, one must determine how to update the optical properties, so a search direction toward the minimum error is determined by the Jacobian and update step size selected. Some common optimization algorithms that have been applied to optical tomography include the Newton–Raphson method, the conjugate gradient method, the truncated Newton method, and Kalman filtering. The reader is referred to treatises of each method described by each of the authors listed in Table 2 as well as to the excellent, comprehensive review by Arridge [52].

**3.2.5 Regularization for formal inversion approaches** In both the integral and differential formulations of the inverse problem, the tissue to be imaged must be mathematically discretized into a series of nodes or volume elements (voxels) to solve these inverse problems. The unknowns of the inverse problems are then comprised of the optical properties at each node or voxel. The final image resolution is naturally related to the density nodes or voxels. However, the dimensionality of the imaging problem is directly related to the number of nodes

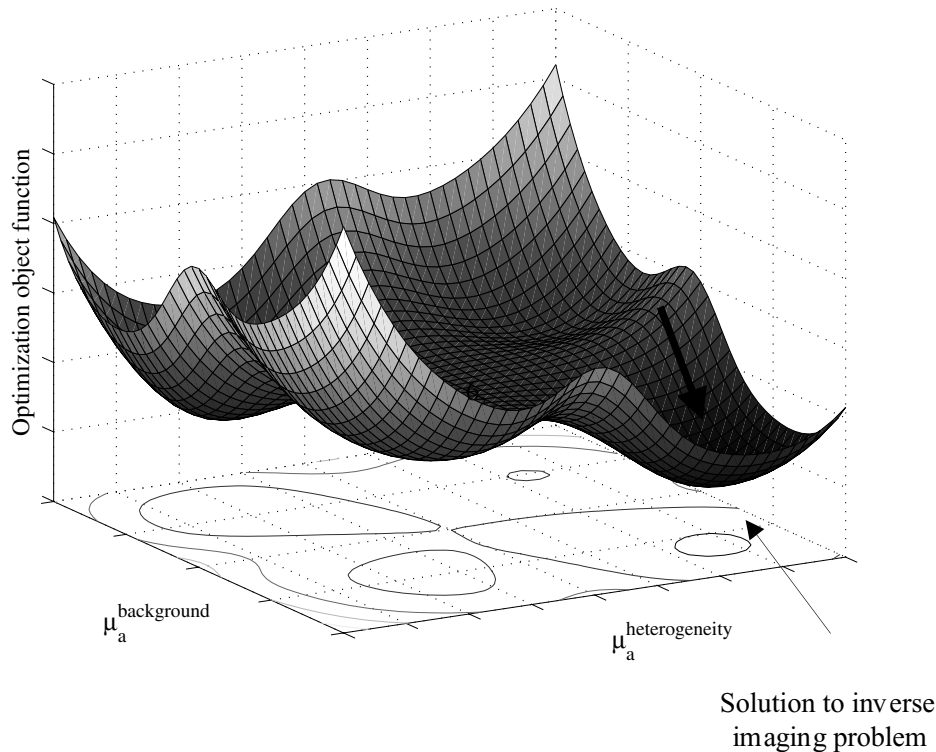


**Figure 6.** Schematic of the formal inversion approach that updates the interior optical-property map using the Jacobian, or the slope of the surface of the error map shown herein, to find the minimum error or “well” that identifies the correct reconstructed image. See text for description.

and can easily exceed 10 000 unknowns for a 3D image. In a problem of this scale, the calculation of Jacobian matrices and matrix inversions involved in updating the optical-property map are computationally intensive and contribute to the long computing times required to reconstruct image, even with modern, powerful computers. Furthermore the solution to the set of ill-posed, linearized equations can be inherently unstable. The instability arises because the measurement noise in the data or errors associated with the validity of the diffusion approximation can result in very large errors in the reconstructed image.

Regularization is a mathematical tool used to stabilize the solution of the inverse problem and to make it more tolerant of measurement error. Regularization approaches will play an important role in the development of suitable algorithms for actual clinical screening. For example when discretized, the differential and integral general formulations result in a set of linear equations generally denoted by  $Ay = z$ , where  $y$  are the unknown optical properties and  $z$  are the measurements. This system is commonly solved in the least squares sense where the object function  $Q = \|Ay - z\|^2 + \lambda \|y\|^2$  is minimized, where  $\lambda$  is called the regularization parameter. The minimization of this function results in  $Y = (A^T A + \lambda I)^{-1} A^T z$ . The regularization parameter is generally chosen either arbitrarily or by a Levenberg–Marquardt algorithm so that the object function is minimized [52]. Thus, the choice of regularization parameter is through *a priori* information and adds another degree of freedom to the inverse problem solution. Although this review is not meant to be a mathematical treatise of inverse algorithm and

regularization approaches, we nonetheless point out that in a recent work by Pogue and coworkers [53] a physically-based rationale for empirically choosing a spatially varying regularization parameter is presented to improve image reconstruction. Likewise, Eppstein and coworkers [28] use actual measurement error statistics to govern the choice of varying regularization parameters in their Kalman filter implementation to optical tomography.

Algorithms that attempt to reduce the computational burden have also been developed or applied to this problem. Such algorithms include reverse automatic differentiation to compute the search direction [33,54], constrained optimization [21], and a novel zonation algorithm that progressively reduces the number of unknowns with each iteration inverse algorithm [28]. The latter case provides a novel solution to the computational intensiveness of solving the inverse problem. At each parameter update, neighboring voxels that possess similar optical properties are merged into one voxel, reducing the number of unknowns to be recovered. Hence during its solution, the convergence is accelerated by moving the problem from one that is underdetermined toward one that is overdetermined. Other approaches to reduce the dimensionality of the problems involve concurrent imaging with MRI [55–57] and ultrasound [58] to compartmentalize tissue volumes and to reduce the number of parameters to be recovered in the optical-image reconstruction.

Owing to the computational intensiveness, the FORWARD and INVERSE models are also typically solved in two dimensions, despite the fact that photons travel in

three dimensions. Methods to deal with this discrepancy involve calibration factors to account for the model mismatch [59] but to date there have been few reported image recovery algorithms tested on actual data using 3D routines [60,61]. Recent developments to solve both the forward and inverse problem in 3D [60–62] have proven successful and promise to provide further progress in image recovery.

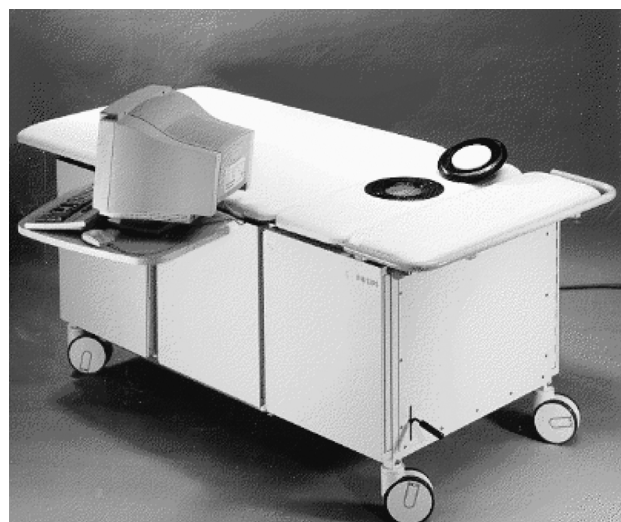
To summarize, the use of NIR techniques requires the use of mathematical forward and inverse formalisms for image recovery. In the following sections, we highlight their use in actual mammographic studies and show the utility of NIR imaging.

### 3.3 Clinical Mammography Studies Using NIR Optical Techniques

Diaphanography, or the imaging of breast tissue using light, was first reported by Cutler [63] in 1929. Owing to the recognition of that NIR light can transit several centimeters and to the serendipitous development of NIR laser diodes, there has been a resurgence of optical mammography developments. In the following, we briefly highlight the application of CW, TDPM, and FDPM to human breast tissue and the use of the image-recovery approaches described above.

**3.3.1 CW optical mammography** Mammographic imaging using CW NIR transmission and backprojection techniques has been accomplished by Philips Medical [44,64]. In their approach, 256 optical fibers are placed at the periphery of a white conical-shaped vessel in which a pendulant breast to be imaged is immersed in a tissue-simulating scattering medium. Three continuous-wave laser diodes are sequentially used to illuminate the tissue through one fiber optic at different positions while the other 255 fiber optics read a transmitted optical signal at separate photodetectors. In total, 65,000 data points are employed in a backprojection algorithm to detect lesions previously identified by conventional X-ray mammography. Figure 7 is an illustration of the clinical scanner developed by Philips, whereas Figures 8 and 9 are the reconstructed images for a 1- to 2-cm mass identified by X-ray mammography as well as a fluid-filled cyst. The images illustrate a common characteristic of all clinical optical tomography: a low-resolution image for detection of rather large tissue masses. In yet another unpublished case, a suspicious tissue region identified by the Philips system indicated hypervascularity, but needle biopsy and conventional X-ray mammography failed to confirm disease. In subsequent patient follow-up, cancer was later found in the hypervascular region previously identified by the optical mammogram (M. B. Van der Mark, 2000, personal communication).

Despite the low resolution, the optical mammograms nonetheless provide images based on endogenous, hemoglobin absorbance contrast that cannot be imaged using other modalities. Other CW mammographic systems are under development including a similar CW optical mammography system and approach developed by Imaging



a)



b)

**Figure 7.** Illustration of (a) the Philips Optical Mammo Prototype system and (b) the detail of the cup area of the unit. The fan of light shows the distribution of the light from a single fiber optic. During data acquisition, which takes about 2 minutes per wavelength, the pendulant breast of the patient is placed in the cup filled with an optically matched fluid. Transmission measurements are then performed by individually shining light into the cup from each of the 255 source fibers. The resultant 255×255 set of transmission measurements are then used for image construction. Reproduced with permission from: <http://www.research.philips.com/generalinfo/special/medopt/mammoscope.html>.

Diagnostic Systems, Inc. (IDSI, Planetarium, FL). While under development, their approach uses backprojection and differential inversion algorithms for image reconstruction and is also under development for TDPM measurement [65].

**3.3.2 TDPM optical mammography** Using the TDPM approach, Grosenick *et al.* [5,66], have evaluated as many as 13 patients with known breast cancers as determined from X-ray, MR- or ultrasound mammography and ranging in size from 0.8 to 2.5 cm in diameter. In their approach, an incident series of light impulses were



delivered to the compressed tissue and the number of photon counts arriving within a selected time-window were used to indicate altered tissue optical properties and therefore evidence of the breast lesion. They also used the solution of the optical diffusion equation for a homogeneous medium to recover absorption and scattering property maps in 2D from the time-of-flight distribution measurements that were made as the source and detector were scanned across the compressed tissue. Scanning measurements of 1 to 2000 data points required 3 to 5 minutes of data acquisition to directly reconstruct an image from a simple backprojection approach. ART, Inc. (Quebec, Canada) is developing a similar compressed tissue scanner that is illustrated in Figure 10.

Upon conducting TDPM measurements at 670 and 785 nm, Grosenick and coworkers demonstrated that better contrast in the measured parameters existed at 670 nm as opposed to those obtained at the wavelength of 785 nm. Their images, like those produced by Colak *et al.* (Ref. [64] and shown in Figures 8 and 9), are diffuse and highlight the contrast due to absorption by an invasive ductal carcinoma. Grosenick *et al.* [5] found that the diseased tissues exhibited approximately 2.5 times the absorption of that of the surrounding normal tissues.

Cubeddu and coworkers [67] also conducted non-imaging mammography experiments on two human subjects using time-domain measurements between a single point source and detector placed in reflectance and transmittance geometries on the breast surface. Their measurements, accomplished as a function of wavelength between 610 and 1010 nm were conducted using a pulsed Ti:sapphire laser and show absorption features of hemoglobin, water, and lipids, which would be expected to provide endogenous contrast for NIR optical mammographic measurements.

**3.3.3 FDPM optical mammography** Mammographic FDPM measurements using a hand-held probe have been recently recorded by Tromberg *et al.* [1] on patients with breast cancer. In the former study, measurements at four different wavelengths were conducted at multiple modulation frequencies and the diffusion equation solution for a homogeneous medium was approximately fit to the data to provide an effective absorption and scattering coefficient of this diseased tissue. While not imaging, *per se*, the study nonetheless further highlights the optical property differences between normal and diseased breast *in vivo* and provides evidence for small changes in tissue optical properties with disease. These optical property changes could form the basis of optical mammography based on endogenous contrast. In a tomographic approach, Holboke *et al.* [58] used ultrasound to locate the tumor and segment the normal breast tissue into compartments that could have differing optical properties. They used four different wavelengths with various modulation frequencies in a parallelized, integral reconstruction algorithm to diagnostically assess the optical properties of the disease. They found that in a single 1.8×0.9-cm ductal carcinoma *in situ* located

7.4 mm beneath the skin, the absorption coefficient was three to four times higher whereas the scattering coefficient was 50% reduced in comparison to the surrounding normal tissues.

In earlier studies, Franceshini *et al.* [68] and Moesta *et al.* [69] used a single point source and detector to conduct FDPM transillumination measurements at 110 MHz using two wavelengths at 690 and 810 nm at 10 mW average power in a raster-scanning geometry across the compressed human breast. Using processed but not inverted FDPM data, they showed the ability to detect a 3-cm-diameter tumor in a 55-year-old patient whose tumor was previously detected using X-ray mammography, and a 0.5-cm primary tumor in a 72-year-old patient whose tumor calcifications were also detected by conventional X-ray mammography. Again, inversion strategies were not attempted in these studies to relate measurements to tissue optical properties, but instead, a map of a single parameter, “N,” was computed from a simple algebraic function of phase delay and amplitude attenuation. The contrast in the calculated FDPM parameter of “N” nonetheless ranged from 4 to 10, providing discrimination of lesions. In yet another study employing the same raster scanning of FDPM measurements at 690 and 825 nm on a compressed breast, the group employed the Born integral reconstruction to identify a 1.6-cm tumor (determined from surgery) from a reconstructed image that rendered a 2.1-cm tumor [34]. Figure 11 is an example of the X-ray mammogram (top figures, craniocaudal and mediolateral) and the optical mammograms (craniocaudal on left, and mediolateral on right) for the 0.5-cm primary carcinoma. Again, the optical mammograms effectively image with low resolution, and provide detection of the large lesions previously identified by conventional X-ray mammography.

In contrast to the hand-held probe and the raster-scanning measurements described above, McBride *et al.* [70] conducted FDPM between point sources and point detectors located in a planar circumference along the surface of the pendulant breast. The gantry of sixteen sources and sixteen detectors is illustrated in Figure 12 along with the schematic of the FDPM measurement. Using light of two wavelengths that are preferentially absorbed by oxy- and deoxy-hemoglobin respectively, McBride *et al.* [70] recorded data at a single modulation frequency of 100 MHz. Employing a 2D differential inversion algorithm, they found that large tumor masses that were detectable by conventional X-ray mammography exhibited up to two-fold increase in absorption coefficient. Figure 13 shows the results of their differential image reconstruction of hemoglobin concentration for an 0.8-cm invasive carcinoma and for a 3.4-cm benign carcinoma in two different patients. Again the diffuse images detect masses that are previously identified by X-ray mammography. Nonetheless, by employing two wavelengths in the spectral region that oxy- and deoxy-hemoglobin absorb, a semiquantitative number reflective of vascular density is obtained. The work suggests the utility of NIR imaging for

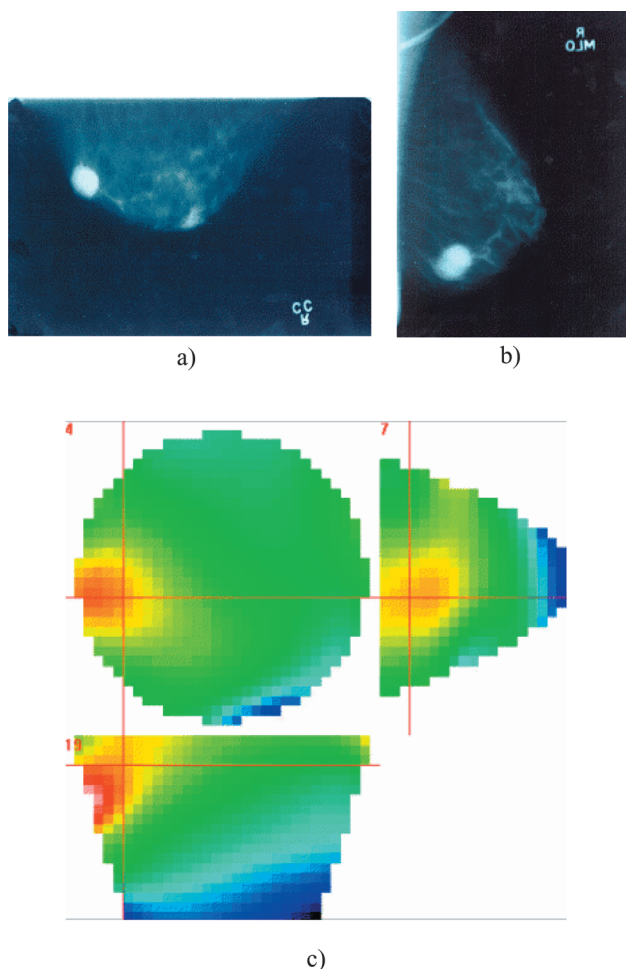


**Figure 8.** Examples of the Philips mammography images for a breast mass of 1 to 2 cm in diameter from conventional X-ray mamograms in the (a) craniocaudal and (b) mediolateral views. The images reconstructed from CW measurements at 780 nm are also shown for the (c) craniocaudal, mediolateral and coronal view images of the same patient. The mass is identified by regions of high attenuation (red). Reproduced with permission from: <http://www.research.philips.com/generalinfo/special/medopt/mammoscope.html>.

assessing the therapeutic benefit of anti-angiogenesis agents currently under clinical trials.

#### 4.0 Fluorescent Contrast Agents for NIR Optical Tomography

Several years have passed since the initial proposals for NIR optical tomography for breast cancer screening using time-dependent measurements of light propagation in the breast. Much accomplishment in the development of optical mammography has been summarized above in Section 3.3, most recently in the application of FDPM [70]; TDPM; [5] and continuous-wave [64] measurements. To date, these NIR techniques predominantly depend on endogenous contrast owing to angiogenesis and increased hemoglobin absorbance for contrast. Although exciting and promising, the necessity of angiogenesis-mediated absorption contrast for diagnostic optical mammography limits the potential for using NIR

techniques for other diagnostic applications such as assessing sentinel lymph node staging, metastatic spread and multifocality of breast disease. Such diagnostics could probably not be done with natural endogenous contrast. In addition, because the endogenous contrast owing to angiogenesis can be expected to be low in small lesions and nonspecific to cancer, there is certainly a limitation for NIR detection of nonpalpable disease in dense breast tissue. Clearly, from the clinical results shown above and the image reconstructions on well-defined phantom studies not reported herein, one can see that the resulting images are of low resolution and are able to discriminate large masses or small phantom volumes contrasted from its surroundings by substantial changes in endogenous optical properties. In addition, the NIR absorption signatures are limited to melanin, oxy- and deoxy-hemoglobin, water, and to a minimal extent, fat. There is some evidence for scattering contrast between normal and diseased tissue, but little work has been done to solve the tomography problem based on scattering contrast alone [1,58]. Hence, the capability for moderately resolved, biochemical molecular imaging within tissues using unassisted NIR optical techniques is somewhat limited and can be expanded through the use of contrast-enhancing agents.

#### 4.1 Mechanisms for Fluorescence, Contrast-Enhanced NIR Imaging

Fluorescent contrast agents have been proposed and independently confirmed as the most efficient means for

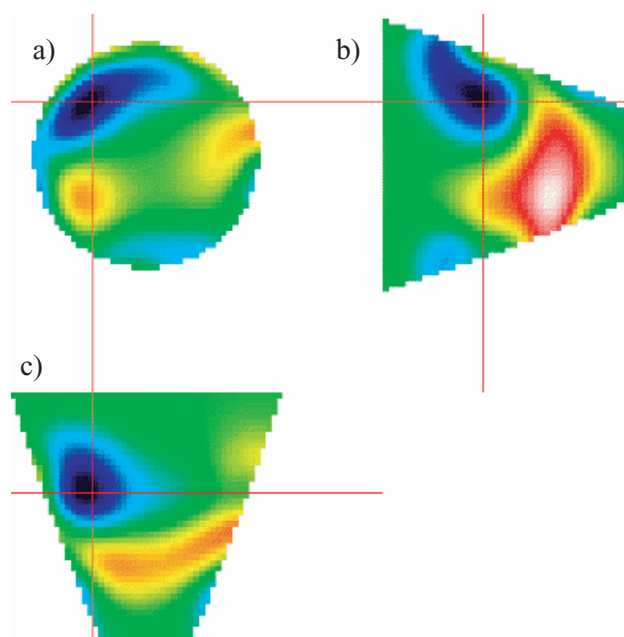


**Figure 9.** Examples of the Philips mammography images for a fluid-filled cyst reconstructed from CW measurements at 780 nm are also shown for the craniocaudal, mediolateral and coronal view images of another patient. In contrast to the optical mammograms illustrated in Figure 8, the fluid-filled cyst is demarcated by regions of low attenuation (blue). Reproduced with permission from: <http://www.research.philips.com/generalinfo/special/medopt/mammoscope.html>.

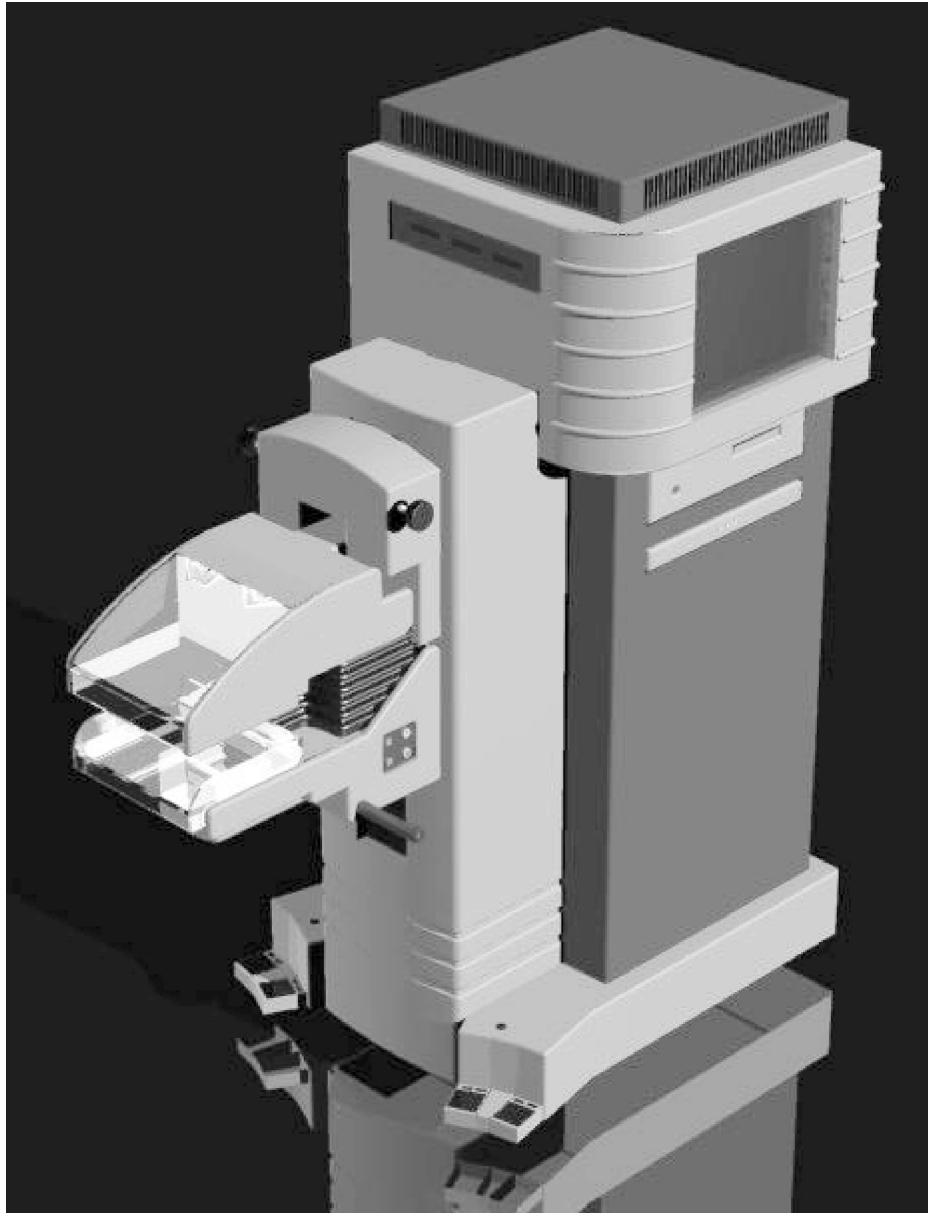


**Figure 10.** An example of the compressed fiber optical scanner from Aerospace Research Technologies, Inc. (ART) that employs scanning of source and detecting fibers for data acquisition. Reproduced with permission from: <http://www.softscan.com/default.html>.

inducing optical contrast when time-dependent measurements are conducted [71,72]. Furthermore, they may in the near future offer a host of opportunities for molecular imaging that is limited only by synthetic design. The basic principles behind fluorescence-enhanced NIR optical tomography is focused first on the kinetics of the fluorescence generation (Figure 14). When a molecule of significant aromaticity absorbs light corresponding to a transitional energy level, it becomes activated into a “singlet” state from where it can relax radiatively, releasing light of lower energy (or higher wavelength) than the incident light. Typically, the fluorescent lifetime,  $\tau$ , (or the mean time that the fluorophore is in the activated “singlet” state) is mediated by the local environment impacting the relative rates of radiative and nonradiative decay to the ground state [73].

Because the fluorescence decay of a given probe can be affected by pH, oxygenation, free ion concentrations, glucose, or other analytes, it can provide an optical assessment of analytes not otherwise directly measurable. Using ratiometric dyes, Mordon *et al.* [74] and Russell *et al.* [75] measured the pH of tissues within a conscious mouse using multiwavelength CW techniques. Oxygen sensitive dyes have also been developed to provide noninvasive measurement of tissue oxygen status [76]. Because fluorescence lifetimes can be directly measured using time- and frequency-domain approaches, a quantitative assessment of the analyte concentration can also be obtained independently from the concentration of the molecular probe, or fluorophore. In addition to fluorescence lifetime, the quantum effi-

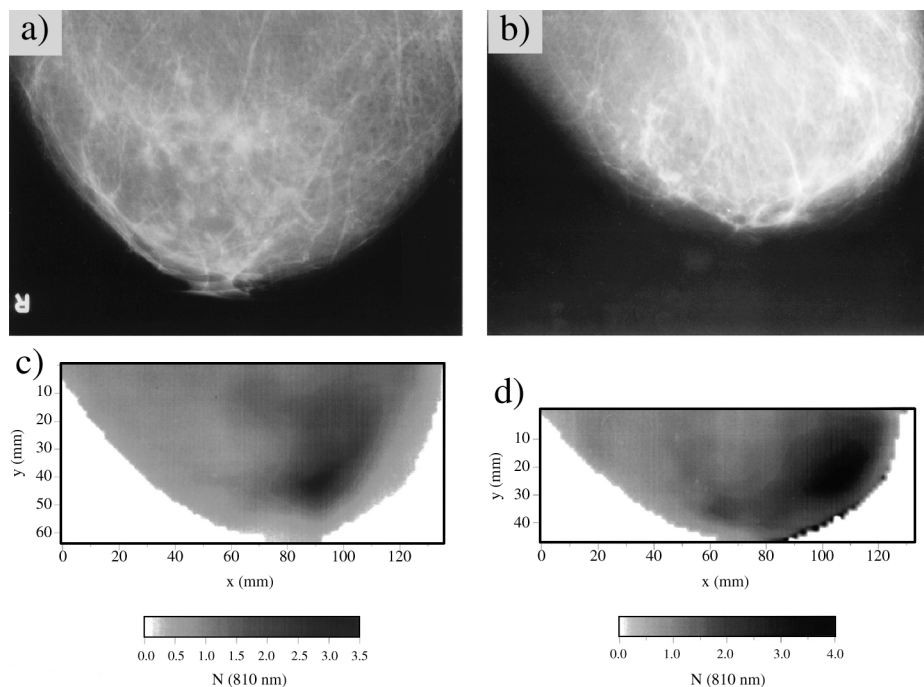


**Figure 11.** X-ray mammograms in (a) craniocaudal and (b) mediolateral views of a 72-year-old woman with invasive ductal carcinoma with a 0.5-cm-diameter primary tumor. The FDPM derived optical mammograms of parameter “N” in (c) cranial caudal and (d) mediolateral views from scanning 810-nm FDPM measurements. Reproduced with permission from Franceschini et al. [68].

ciency, or the amount of fluorescence light generated per unit light absorbed can also be assessed using continuous-wave techniques.

Fluorescence-enhanced NIR imaging is accomplished when propagating excitation light activates exogenous fluorescent agents within the tissue. The generated fluorescent light propagates through the tissue to its surface where an interference filter enables detection of the scattered fluorescent light and the rejection of the multiply scattered excitation light. Typically, the greater the ratio of exogenous fluorescent agent in the tissue volume of interest to that in the surrounding tissues, the greater the contrast for image reconstruction. However, in the case of time-dependent measurements, it is the kinetics that create a nanosecond or subnanosecond time-lag between absorption of excitation light and generation of fluorescent light that provides additional contrast for imaging. However, it is important to note that the enhanced contrast is at the expense of signal to noise ratio (SNR) when TDPM or FDPM approaches are employed. Using experimental FDPM measurements in phantom studies, we have found that the contrast, or measured phase and amplitude attenuation change, of a propagating, fluorescent photon density wave generated from within tissue-simulating media exceeds that due to its excitation counterpart, even in the presence of a perfect, black absorber [77]. Similar results have been predicted theoretically [77,78]. Using continuous-wave transillumination measurements in phantom studies, Zhu and coworkers [79] focused on the absorption features rather than the fluorescent features of contrast agents. Although they show that contrast can be imparted using two wavelengths at which the exogenous nonfluorescing dye does

and does not show appreciable absorption cross section, their results may be compromised in tissues when operating at a wavelength where hemoglobin also has significant absorption.

Figure 15 provides a simple schematic describing the physics behind why fluorescent contrast is greater than that possible by absorption for FDPM imaging. Consider a tissue volume illuminated by an intensity modulated light source at source position,  $r_s$ . The propagating wave is denoted with solid lines. As the propagating excitation wave transits through the tissue, it is attenuated and phase-delayed owing to the tissue optical properties. If the wave encounters a light absorbing heterogeneity, such as a highly vascularized tumor, a portion of the intensity wave is reflected. The strength of the “reflected wave” (or dotted line) is dependent on the absorption contrast, the size and depth of the heterogeneity. This “reflected wave” makes a small contribution to the wave that ultimately is detected at detector position  $r_d$ . It is this small, added contribution that is used to detect the heterogeneity. If the added contribution is not within the measurement noise, then it provides information for image recovery in one of the inversion strategies outlined above. However, if the heterogeneity were contrasted by fluorescence, then upon reaching the heterogeneity, the excitation wave generates an emission wave (solid lines). The emission wave then acts as a beacon and upon employing an interference filter to reject the excitation light, can be measured to directly locate the heterogeneity. In small tissue volumes, such as the mouse or rat, inversion algorithms may not be required to detect the fluorescent heterogeneity. However, in larger

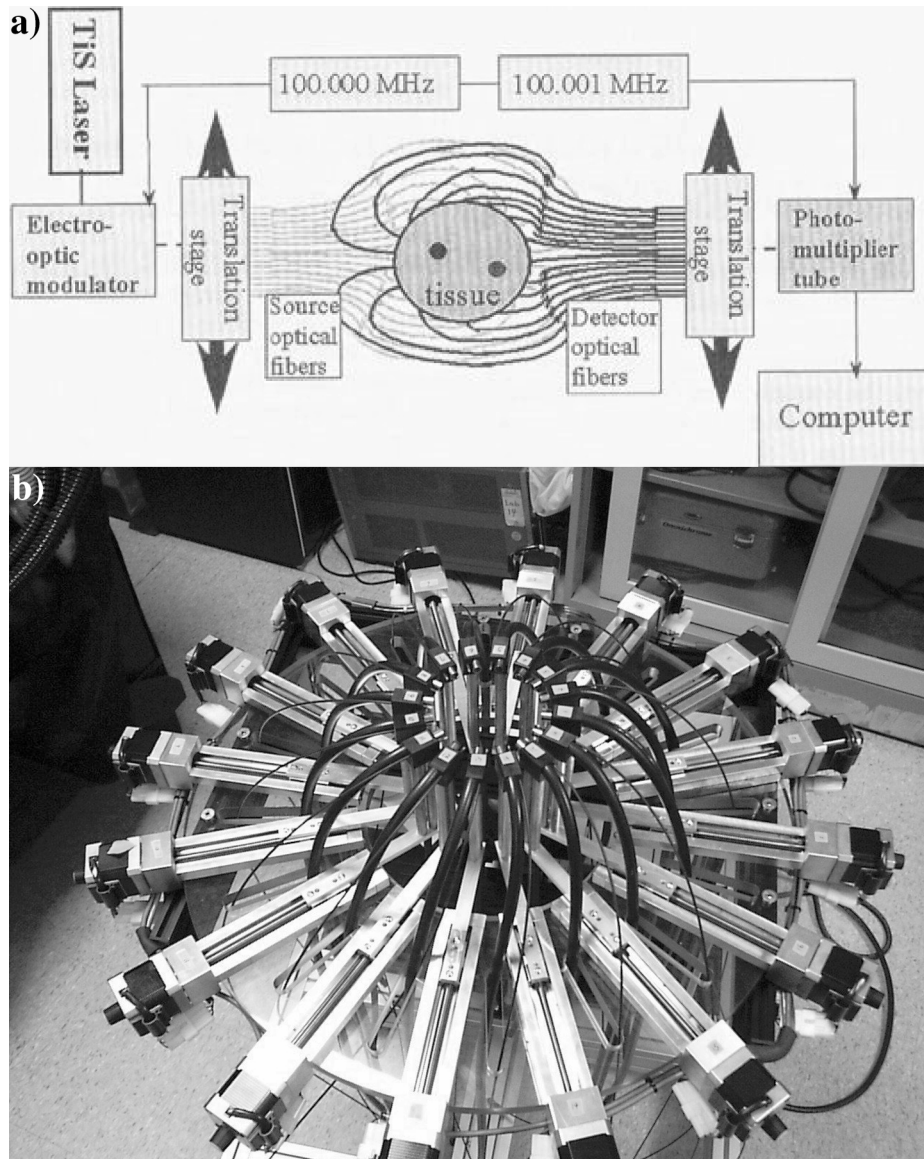


**Figure 12.** The (a) schematic and (b) photograph of the Dartmouth mammographic imaging system that utilizes a CW Ti:sapphire laser with an electro-optic modulator to produce intensity-modulated incident light at 100 MHz and variable wavelength. The source light is coupled sequentially into 16 individual fibers positioned on the circumferential surface of a pendant breast and the light that propagates through the tissues is detected by another 16 fiber optics, which is coupled sequentially into a detector. The set-up allows for variable diameter of the circumferential gantry of fiber optics and its vertical translation. Illustration reproduced with permission from McBride et al. [70] and photograph provided by B. Pogue.

tissue volumes, the forward and inverse imaging problems require solution for effective image recovery. Finally, because a fluorescent probe can be “tuned” to exhibit differing fluorescence decay characteristics dependent on its local environment, the re-emitted signal can contain diagnostic information about the tissue of interest.

Fortunately, or unfortunately, as the case may be, endogenous molecules are not fluorescent when excited by red light. Hence exogenous contrast agents are required. In the following sections, we outline the principles behind fluorescent contrast agents for optical tomography using CW, FDPM, or TDPM measurements; the solutions to the forward and inverse imaging problems; and the advantages to using fluorescence contrast agents. Finally, we summarize the limited *in vivo* studies employing fluorescence contrast agents and conclude this review with a prognosis

for the development of optical mammography in particular and of NIR optical tomography of tissues, in general. Sections 4.1 and 4.2 are included for completeness, but may be omitted without loss of comprehension for those readers less mathematically inclined.

#### 4.2 Solution to the Forward Contrast-Enhanced Imaging Problem

**4.2.1 CW contrast-enhanced imaging** Because red light multiply scatters as it transits tissues, it has the opportunity to excite fluorescent contrast agents that in turn act as a source of fluorescent light. If the fluorescent contrast agent partitions exclusively within the tissue of interest, the fluorescent light can be a “beacon” providing direct localization of the diseased tissue volume. If the contrast

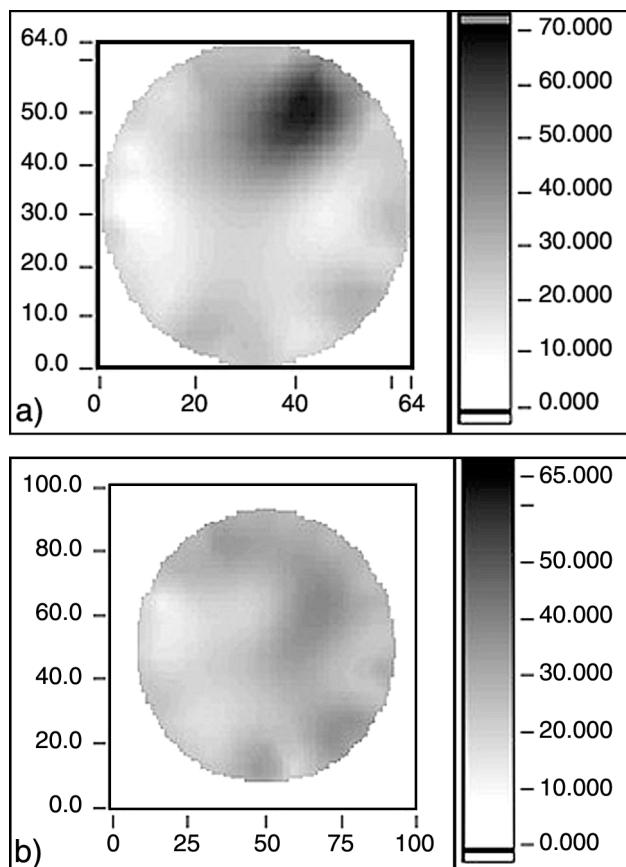


**Figure 13.** Two-dimensional reconstruction from data gathered in the apparatus described in Figure 12 for (a) a patient with a 0.8-cm-diameter invasive carcinoma in tissues surrounded by the 6.4-cm-diameter gantry of sources and detectors, and (b) the normal contralateral breast. The scale bar is calibrated hemoglobin concentration in micromolar units. The position of increased hemoglobin concentration coincides with the locations identified by the radiologist. Provided by B. Pogue.

agent does not partition exclusively in the tissue volume of interest; then forward and inverse solutions are necessary. In either case, two optical diffusion equations for time-invariant excitation light propagation and emission light generation and subsequent propagation are used to solve the forward solution. The diffusion equation for excitation light (Equation 1) provides solutions for the excitation fluence,  $\Phi_x$ , whereas the optical diffusion equation for emission light is written:

$$\nabla \cdot D_m(\vec{r}) \nabla \Phi_m(\vec{r}) - \mu_{a_m}(\vec{r}) \Phi_m(\vec{r}) = -\phi \mu_{a_{ex}}(\vec{r}) \Phi_x(\vec{r}) \quad (6)$$

Here  $\Phi_m$  is the fluence at the emission wavelength;  $\mu_{a_{ex}}$  is the absorption coefficient at the excitation wavelength owing to the fluorophore distributed within the tissue; and  $\mu_{a_m}$  is the absorption coefficient at the emission wavelength. In Equation 6, it is assumed that photobleaching is inconsequential and re-absorption of the fluorescent light by the fluorophore is minimal, i.e., the fluorophore exhibits a small absorption cross section at the emission wavelength. Nonetheless, these effects of photobleaching at high incident light powers and re-absorption can be easily accounted for in the diffusion equations. In the correspond-

ing equations for excitation light propagation (Equation 1), the absorption coefficient,  $\mu_a$ , becomes equivalent to the sum of absorption owing to endogenous chromophores,  $\mu_{a_{ex}}$ , and the absorption owing to the fluorophore,  $\mu_{a_{fl}}$ . The isotropic scattering coefficient at the excitation wavelength,  $\mu'_{s_x}$ , may also be different than the coefficient,  $\mu'_{s_m}$ , at the emission wavelength. Consequently, the optical diffusion coefficients at the excitation and emission wavelengths,  $D_x$  and  $D_m$ , can be expected to differ. To predict the emission fluence,  $\Phi_m(\vec{r})$ , one is first required to solve the excitation diffusion Equation 1 for the distribution of excitation fluence,  $\Phi_x(\vec{r})$ , for use in the source term of the emission diffusion Equation 6. The same boundary conditions used for solution of the excitation fluence are also used for solution of the emission diffusion equation.

It is important to note that fluorescence-enhanced continuous-wave imaging cannot probe tissues if the agent does not partition exclusively within the tissue volume. The reason lies with the dependence of the local concentration of activated fluorophore, which is proportional to the product of the excitation light fluence,  $\Phi_x$ , (which exponentially attenuates with increasing distance from the source within the tissue) and the local concentration of fluorophore. In the absence of photobleaching, the origin of fluorescent signals detected at the tissue-air interface will predominate from tissue regions with the highest concentration of *activated* fluorophore — which in the case of continuous-wave illumination, remains at the tissue surface. Even with residual concentrations of fluorophore at the tissue surface, NIR emission light resulting from noninvasive excitation light illumination will not originate from beyond a few millimeters of tissue owing to the overwhelming excitation light fluence of the interface. Hence, simply because a fluorescent probe excites in NIR does not imply that it can be used for deep imaging.

**4.2.2 TDPM contrast-enhanced imaging** For systemic administration of fluorescent contrast agents, TDPM or FDPM measurements may be required to interrogate deep tissue volumes. In the time-domain approaches, an excitation impulse propagates through the tissue and, when it reaches a fluorophore, produces an impulse of emission light that propagates spherically within the tissue. The governing equation describing excitation light propagation is provided by Equation 1 above, whereas the emission light propagation is predicted by the following expression (for details see Refs. [80,81]):

$$\frac{1}{c} \frac{\partial \Phi_m(\vec{r}, t)}{\partial t} - \nabla \cdot D_m \nabla \Phi_m(\vec{r}, t) + \mu_{a_m}(\vec{r}) \Phi_m(\vec{r}, t) - \frac{\phi \mu_{a_{ex}}}{\tau} \int_0^t \exp\left[-\frac{(t-t')}{\tau}\right] \Phi_x(\vec{r}, t') dt' = 0 \quad (7)$$

Again, the excitation light fluence,  $\Phi_x(\vec{r}, t)$  is predicted by Equation 1 wherein the absorption coefficient at the excitation wavelength,  $\mu_a$ , becomes equivalent to the sum of absorption

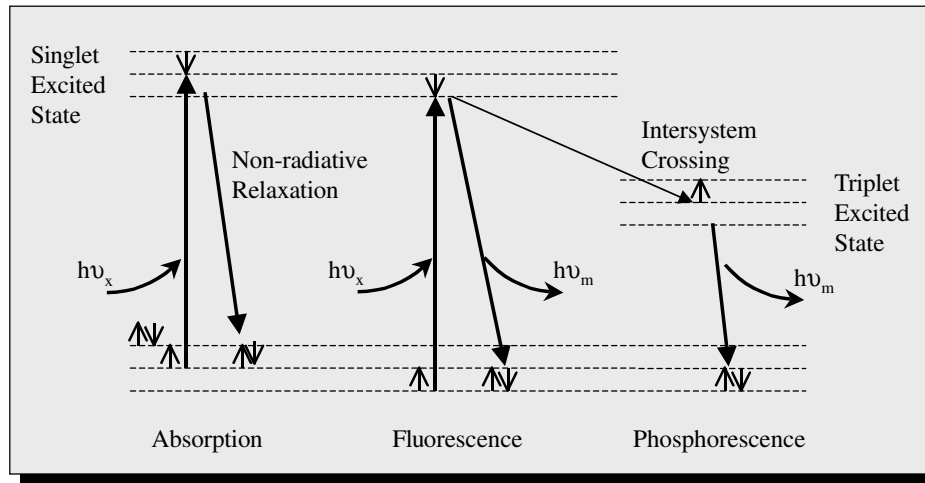


**Figure 14.** The Jablonski diagram illustrating the activation of fluorophore to its single excited state and its nonradiative and radiative (fluorescence) relaxation to the ground state. The fluorescence lifetime,  $\tau$ , is equivalent to the mean time that the fluorophore remains in its activated state and the quantum efficiency is the proportion of relaxations that occur radiatively. In PDT agents, the singlet excited state can undergo “intersystem crossing” in which the spin state of the electron is flipped. Relaxation of the triplet excited state is forbidden until the electron spin state is reversed. The lifetimes of the triplet state are on the order of microseconds to milliseconds and are termed phosphorescence.

owing to endogenous chromophores,  $\mu_{a_{xt}}$ , and absorption owing to the fluorophore,  $\mu_{a_{xt}}$ . Equation 7 assumes first-order single-exponential fluorescent decay kinetics, whose time constant is the fluorescence lifetime,  $\tau$ . Equation 7 can be easily relaxed to include multiexponential decay kinetics [82] and re-absorption phenomena. Typically, owing to the integral in Equation 7, TDPM assessment of fluorescent decay kinetics in scattering media is not generally employed. To alleviate the difficulty, a new approach to model NIR

fluorescence generation and propagation using random walk theory has been developed [83,84].

Here again, if the agent is not exclusively localized within the deep tissue volume of interest, then long-lived contrast agents (such as phosphorescent agents) located even in vanishingly small concentrations at the tissue interface will be the predominate source of detected emission light. However, if agents have fluorescent lifetimes smaller than or on the same order as the nanosecond photon times-of-

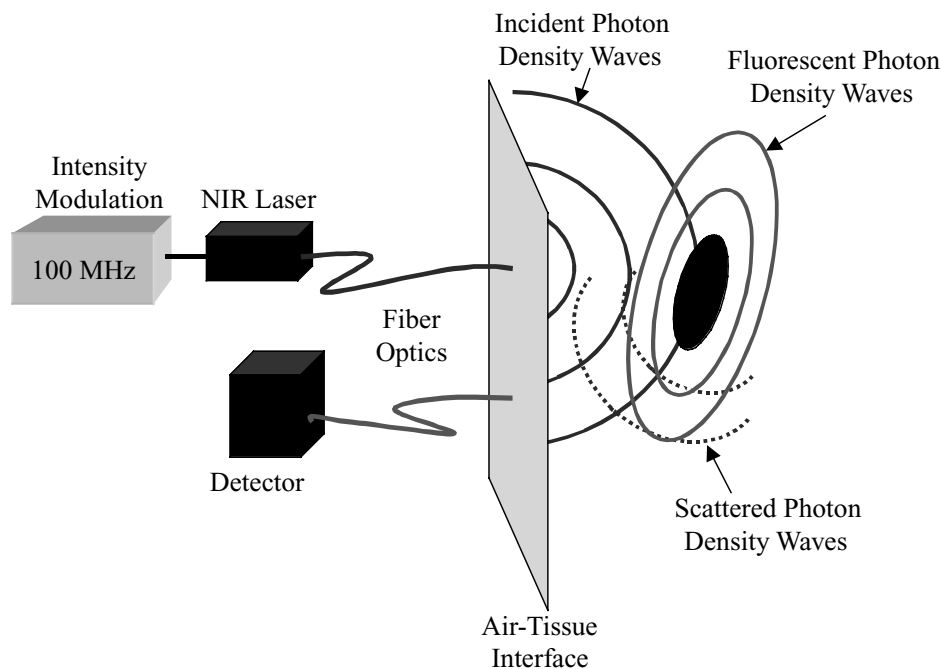


**Figure 15.** Schematic detailing the propagation of excitation photon density waves (solid lines) and their perturbation by absorbing heterogeneities (dotted lines) and the generation of emission photon density waves (solid, grey lines) within tissues. Fluorescence contrast-enhance optical tomography provides greater localization capability because the detected emission waves act as “beacons” providing information regarding the tagged heterogeneity.



flight, then the emission from activated fluorophores at the tissue–air interface will attenuate rapidly as the pulse of excitation light propagates deeper and activates fluorophores located in deeper regions of the tissue. In summary, efficient contrast agents administered systemically must have nanosecond or subnanosecond lifetime kinetics to be effective in deep tissues [80].

**4.2.3 FDPM contrast-enhanced imaging** Similar arguments are *en force* in the frequency-domain approach whereby an intensity-modulated wave of excitation light propagates to a fluorescent dye, which upon excitation and subsequent relaxation re-emits a fluorescent intensity wave that possesses additional phase delay and amplitude attenuation owing to the fluorescence decay kinetics. The equation describing the generation and propagation of a fluorescent wave is given by [85,86]:

$$\nabla \cdot D_m(\vec{r}) \nabla \Phi_m(\vec{r}, \omega) - \left[ \mu_{am}(\vec{r}, \omega) + i\omega/c \right] \Phi_m(\vec{r}, \omega) + \Phi \mu_{axf}(\vec{r}) \frac{1 - i\omega\tau(\vec{r})}{1 + \omega^2(\vec{r})\tau^2}(\vec{r}) = 0 \quad (8)$$

Again, to solve Equation 8 for the complex emission fluence,  $\Phi_m(\vec{r}, \omega)$ , the complex excitation fluence,  $\Phi_x(\vec{r}, \omega)$ , must first be computed from Equation 4. Here again, the optical properties at the excitation and emission wavelengths should be expected to differ and the boundary conditions used for solution of the complex excitation fluence are also used for solution of the complex emission fluence. The complex emission fluence,  $\Phi_m(\vec{r}, \omega)$ , is measured at the air–tissue interface in terms of a phase delay,  $\theta_m$ , and amplitude attenuation,  $M_m$ , relative to the incident excitation source.

The coupled diffusion equations (4) and (8) have an analytical solution when absorption, scattering, and fluorescent properties at excitation and emission wavelengths are spatially constant in a homogeneous scattering medium [85–87]. Using FDPM measurements at both excitation and emission wavelengths, the ability to measure the single exponential lifetimes of indocyanine green (ICG) and 3,3'-diethylthiatricarbocyanine iodide (DTTCI) in scattering media [88] and rhodamine B [89] in tissue-like scattering media of intralipid 90 has been demonstrated experimentally. The challenge to reconstruct images of fluorescently marked tissue from experimental measurements of multiply scattered light remains to be met.

### 4.3 Solution to the Inverse Contrast-Enhanced Imaging Problem

As described in Section 3.2, there are few studies that successfully invert NIR tissue optical measurements to render images of endogenously contrasted tissue volumes. Owing to the translation of diagnostic fluorescent dyes into the clinic, currently there are even fewer studies employing fluorescent contrast agents. Nonetheless, several investigations have employed synthetic data sets and phantom studies as outlined in Table 3 using localization [7,90,91], backpropagation [92], differential [26,28,29,33,93,94] and integral reconstruction approaches [95,96]. Basically, the approaches are similar to those previously described with the exception of three points: 1) owing to the low quantum yield of fluorescent dyes, the SNR for continuous-wave, time- and frequency-domain measurements is inarguably lower, potentially making it more difficult to successfully reconstruct images [96]; 2) owing to the fluorescence lifetime delay, both TDPM and FDPM approaches have additional contrast in the time-dependent photon migration characteristics, potentially making the technique more sensitive for detection of smaller tissue volumes [77]; and finally 3) owing to the ability to directly invert the fluorescence kinetic parameters of fluorescence lifetime and quantum efficiency, the technique can be used to perform specific molecular imaging through enzyme-catalyzed reactions, or receptor–ligand binding. The latter characteristic of fluorescence lifetime imaging reveals its similarity to magnetic resonance imaging (MRI). In MRI, imaging is accomplished by monitoring the RF signal arising from the relaxation of a magnetic dipole perturbed from its aligned state using a pulsed magnetic field. In fluorescence contrast-enhanced optical tomography, the imaging is accomplished by monitoring the emission signal arising from the electronic relaxation from an optically activated state to its ground state. Unfortunately, the emission light is multiply scattered, hence the resolution afforded by MRI is unlikely to be matched by contrast-enhanced optical tomography. Unlike contrast agents for conventional imaging modalities, optical contrast owing to fluorescent agents may be imparted in two ways: 1) through increased tumor:normal tissue concentration ratios, and 2) through alteration in the fluorescence decay kinetics upon partitioning within tissue regions of interest.

Several investigators have demonstrated the feasibility of fluorescence contrast-enhanced NIR imaging. Hull *et al.* [91] employed spatially resolved reflectance measurements

**Table 3.** Survey of Literature Work Involving the Solution of the Inverse Contrast-Enhanced Imaging Problem.

Author	General inversion formulation	Data type	Noise considered?	2D or 3D	Forward method	Meas. mode
Wu <i>et al.</i> [90]	Localization	Phantom	Yes	3D	None	TDPM
O'Leary <i>et al.</i> [142]	Localization	Phantom	Yes	3D	None	TDPM
Schotland [92]	Backprojection	Simulated	No	3D	None	CW
Paithankar <i>et al.</i> [26]	Differential (Newton–Raphson)	Simulated	Yes	2D or 3D	MFD	FDPM
Chang <i>et al.</i> [93,94]	Differential (conjugate gradient)	Simulated	Yes	2D or 3D	NS	CW/FDPM
Roy and Sevick-Muraca [33]	Differential (gradient-based optimization)	Simulated	Yes	2D or 3D	FEM	FDPM
Eppstein <i>et al.</i> [143]	Differential	Simulated	Yes	3D	MFD	FDPM
Eppstein <i>et al.</i> [28]	Differential	Simulated	Yes	2D	MFD	FDPM



and Boas *et al.* [7] conducted FDPM measurements to show that they could locate the origin of a fluorescent heterogeneity in three dimensions when no fluorophore was present in the “background” or simulated surrounding tissues. Using the differential approach, Paithankar and coworkers [26,72] were able to reconstruct lifetime as well as the absorption coefficient owing to the fluorophore,  $\mu_{a_{xf}}$ , from FDPM measurements. Their approaches were effective when the fluorescent contrast agents were distributed throughout the simulated tissue. Subsequently, O’Leary *et al.* [95], Chang and coworkers [93,94], and Eppstein and coworkers [28,62] employed integral and differential approaches to recover fluorescent lifetime as well as absorption coefficient  $\mu_{a_{xf}}$ . Unlike the inverse imaging problem described in Section 3.2, the fluorescence contrast-enhanced imaging problem is linear and as a result, imparts advantages for image recovery [98]. Although the recovered images of fluorescence lifetime and absorption coefficient have been diffuse, they have nonetheless succeeded in detection of small volumes on the order of 0.125 cm<sup>3</sup> [97,98]. Figure 16 shows the 3D image recovered from synthetic fluorescence measurements using the differential approach coupled with the Bayesian-based APPRIZE technology. It shows the ability of APPRIZE to clearly distinguish in three dimensions numerous and small heterogeneities in the presence of “background” fluorophore. The reconstruction was accomplished with eight NIR sources (on one side) and 90 detectors in both reflectance and transillumination geometries on a simulated, compressed breast. The fluorophore exhibiting a 10-fold uptake [(concentration inside region)/(concentration outside region)=10] in the five regions shown in Figure 16, are distinctly recovered from FDPM simulated measurements of phase. Although full reconstructions from experimental phantom data have been reported [98], the challenge remains to increase the SNR, which tends to offset the increased contrast owing to fluorescent agents [96].

Using synthetic FDPM data with appropriate noise added to mimic experimental measurements conducted in our laboratory, Roy used constrained optimization techniques to reconstruct three fluorescently labeled heterogeneities within a frustum geometry that approximates the geometry used in the clinical study [21]. Using 43 sources and 42 detectors located at the surface of the frustum at varying heights, the images reconstructed in three dimensions match well the actual situation without the “blurring” or diffuse imaging prevalent in NIR tomography based on endogenous absorption. Panels (a) through (c) of Figure 17 illustrates the actual “heterogeneities” whereas panels (d) through (f) illustrate the reconstructed images.

Although FDPM measurements of fluorescence are mathematically easier to invert (i.e., for those mathematically inclined readers, see the integral in Equation 7), there has been some work toward developing an approach for time-resolved fluorescence contrast-enhanced NIR imaging. Lyubimov [99] developed the mathematical framework for tomographic reconstruction of fluorescent inclusions embedded in tissue-scattering media on the basis of time-

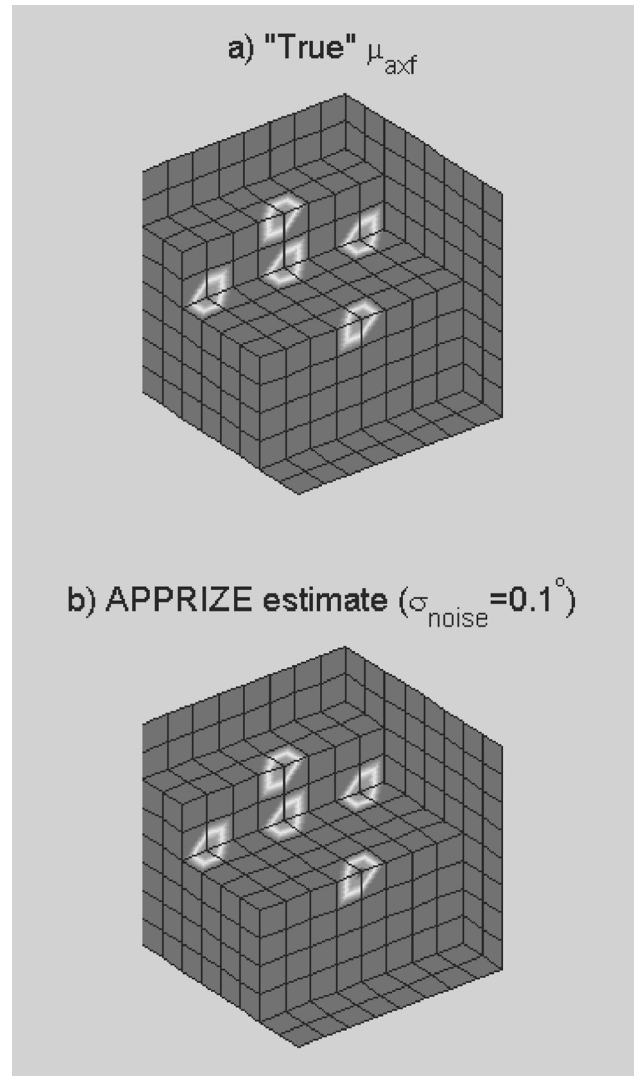


**Figure 16.** Solution of the FORWARD and INVERSE imaging problems for a 4×4×4-cm simulated tissue phantom with eight NIR sources in planar geometry and 90 detectors distributed on the same plane as the sources and distributed on the opposite plane in transillumination geometry. Panel (a) shows the actual distribution of absorption owing to fluorophore with a 10:1 uptake in five heterogeneities of approximately 5-mm diameter. Panel (b) illustrates the image reconstruction accomplished through APPRIZE Bayesian technologies using phase measurements with ample noise. Panel (b) required little more than 4 minutes on a 350 MHz Pentium II PC to compute. Provided by M. Eppstein.

domain or mean photon paths whereas Chenomordik *et al.* [83] have re-poised the forward and inverse solution to the fluorescence imaging problem using random walk theory.

The area of inversion strategy for contrast-enhanced image recovery is relatively new and promises future breakthroughs that are not possible with optical tomography without the use of fluorescence. In the following section, we highlight the recent advances in developing fluorescent agents and review their use in animals.

#### 4.4 Fluorescent Contrast Agents for NIR Optical Tomography

**4.4.1 Indocyanine green dye** Although many advances in dye development have accelerated within the past two years,

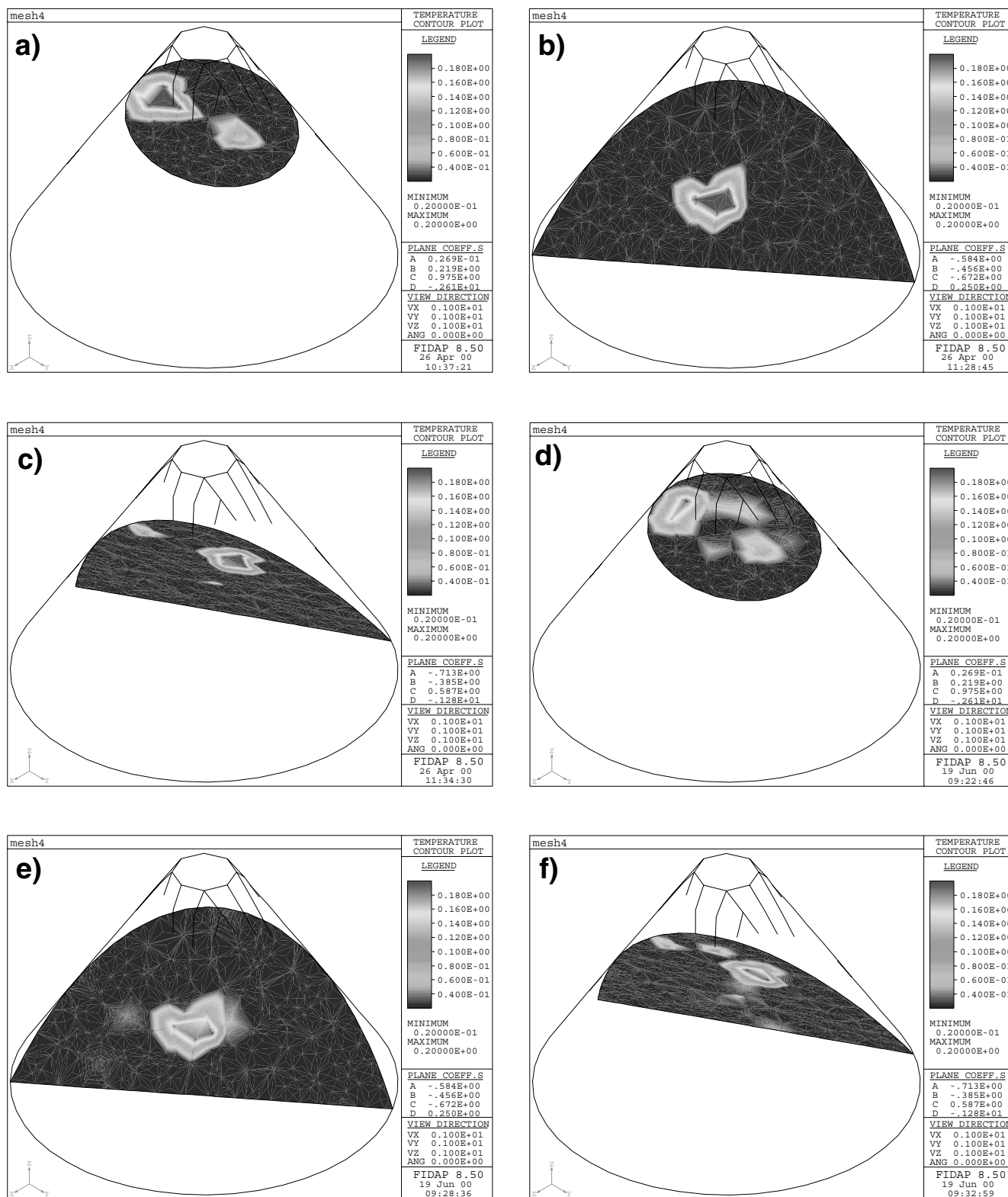


**Figure 17.** Demonstration of three-dimensional reconstruction of 10-fold uptake in three heterogeneities each occupying 0.04% of the total volume of a frustum. Panels (a) through (c) illustrate the true image represented as "slices" through the three-dimensional geometry whereas panels (d) through (f) illustrate the recovered images using synthetic emission FDPM measurements with 35-dB SNR. Using 43 sources and 42 detectors located at the surface of the frustum at varying heights, the images reconstructed in three dimensions match well the actual situation without the "blurring" or diffuse imaging prevalent in NIR tomography based on endogenous absorption. Provided by R. Roy.

the majority of studies investigating NIR fluorescent contrast agents are restricted to ICG, a compound with FDA approval

for systemic administration. ICG is excited at 780 nm and emits at 830 nm. It has an extinction coefficient of 130,000

$M^{-1} \text{ cm}^{-1}$ , a fluorescent lifetime of 0.56 ns, and a quantum efficiency of 0.016 for the 780/830-nm excitation/emission wavelengths in water [77]. It should be noted that these values are not necessarily what will be observed *in vivo*.

When dissolved in blood, ICG binds to proteins such as albumin and lipoproteins. The absorption maximum shifts up to 805 nm but the wavelength of maximum fluorescence is stable near 830 nm, and the fluorescent intensity is dependent on its concentration [100,101]. ICG is a nonspecific agent and is cleared rapidly from the blood, but tends to collect in regions of dense vascularity through extravasation [102].

Using an image-intensified camera to detect continuous wave as well as FDPM images of phase delay and amplitude attenuation, Reynolds *et al.* [103,104] and Gurfinkel *et al.* [102] tracked the uptake and distribution of ICG in spontaneous canine mammary tumors following IV systemic administration. Because canines are the only other species to naturally encounter mammary and prostate cancer besides man [105], this is an excellent animal model in which to assess the potential of detecting diseased tissue through a contrast agent.

In our measurements of the canine mammary chain, we employed a gain-modulated image intensifier as a homodyned, multipixel radiofrequency phase-sensitive camera. The use of a gain-modulated image-intensified charge-coupled camera (ICCD) was first introduced by Lackowicz and Berndt [106] for nonscattering systems and subsequently applied to FDPM imaging of absorbing in scattering phantoms [107]. Essentially, instead of detecting the light that has propagated to a point or series of points on the tissue surface, the ICCD system acts as an area detector, collecting the spatially distributed light re-emitted from the tissue surface. In the case of the anesthetized canine (Figure 18) we scanned the mammary chain using the ICCD area detector to collect the emitted fluorescence owing to ICG. Excitation was accomplished by illuminating the tissue surface with a 4-cm-diameter expanded beam of a 20-mW, 780-nm laser, which was modulated at 100 MHz. Figure 19 shows the DC, amplitude, phase, and modulation ratio (AC/DC) of 830-nm wavelength emitted from the left fourth mammary gland with a palpable 1.2-cm (longitudinal) by 0.5-cm (axial) papillary adenoma located approximately 1 cm deep within the mammary tissue. The image was acquired 23 minutes following IV injection of 1 mg/kg ICG. The diseased region is clearly shown in the raw, unprocessed DC, amplitude, phase, and modulation images. Figure 20 is another *in vivo* image acquired cranial to the nipple of the left fifth gland 30 min after ICG injection. Although the imaged area was not associated with a palpable nodule, pathologic examination confirmed that the fluorescence was attributed to a blood vessel that bifurcated approximately 1 cm below the tissue surface in an area cranial to a regional lymph node. Figure 21 represents the *in vivo* FDPM images of the fluorescence generated from the area of the right fifth mammary gland 43 min after injection of the ICG. Pathologic examination showed that the fluorescent source in this image corresponds to the regional lymph node.

The ability to detect fluorescence signals originating from regional lymph nodes suggests that FDPM fluorescence imaging coupled with improved fluorescent dyes can provide a valuable diagnostic method for assessing regional lymph node status in patients with breast cancer. Lymph node status in patients with breast cancer can be a powerful predictor of recurrence and survival, and the number of lymph nodes with metastases provides crucial prognostic information regarding the choice of adjuvant therapy [108]. Currently, lymph node involvement is assessed by dissection and subsequent pathologic examination, but researchers are investigating the use of other diagnostic modalities including MRI, X-ray computed tomography, and sonography [108]. More recently, gamma ray imaging of a technetium-99 sulfur colloid injected into the tissue area of a known breast tumor has been used to identify the sentinel lymph nodes that, with the simultaneous or sequential injection of a blue dye to visually aid surgeons, can be surgically removed [109,110]. Moreover with NIR fluorescent agents, sentinel lymph node mapping could possibly be achieved without the use of the radionuclide nor with the introduction of a second dye to aid in surgical incision. Furthermore, with the development of peptide, protein, or antibody conjugated fluorescent dye described below, there exists the potential for nonsurgical, optical diagnosis of nodal involvement.

The use of ICG for optical tomography has already been identified by the Chance group at the University of Pennsylvania. In a combined time-domain and MRI-imaging study of 11 patients, Ntzachristos *et al.* [55] administered 0.2 mg/kg ICG IV and conducted measurements in response to pulsed excitation at 780 nm. Their system involved pulsed laser diodes at 780 and 830 nm multiplexed into 24 source fibers and collected at eight detection points [111]. Using the MRI images to validate their integral inversion results, they were able to reconstruct images of an infiltrating ductal carcinoma owing to the enhanced signature from the vascular blood pooling of ICG. Unfortunately, fluorescence signals were not acquired, due possibly to the low SNR available with TDPM measurements, and the images were reconstructed from signals at the incident wavelength.

**4.4.2 Derivatives and conjugates of ICG** Owing to its approved use and optimal excitation and emission maxima at 780 and 830 nm, the best candidate for an NIR fluorescent contrast agent to date remains ICG and its derivatives. Using an ICG derivative labeled with antihuman carcinoembryonic antigen monoclonal antibody, Maguruma and coworkers [112] showed through immunohistochemical staining that targeted delivery of the fluorophore in the digestive tract could enable novel, endoscopic detection of micro cancers. Upon injecting ICG bound to purified lipoprotein into subarachnoid space of the neonatal rat, Sakanti *et al.* [113] used a cooled CCD camera to detect the fluorescence in the subarachnoid space and cerebrospinal fluid pathways *in vivo*. Becker and coworkers [114,115] coupled the peptide transferrin to indotricarbocyanine to facilitate cellular uptake and internalization into tumor cells overexpressing the transferrin receptor. Coupling these cyanine dyes to



different acid-cleavable hydrazone links that were bound to peptides, proteins, and antibodies, this group furthermore sought to develop a pH-sensitive contrast agent whose fluorescence is mediated by tumor acidosis [116]. More recently, Achilefu and coworkers [117] compared the retention of ICG and its derivatized analogue, cypate, with the receptor-specific peptide–cypate conjugate (cytate) in a rat tumor model. They show that receptor-mediated uptake results in as much as a 17:1 tumor:muscle fluorescence contrast using imaging techniques.

**4.4.3 Photodynamic therapy (PDT) agents** Although photodynamic agents are typically designed to exhibit triplet states that will form cytotoxic products in the presence of oxygen, several exhibit radiative relaxation from the singlet state, or fluorescence. Indeed, Pandey and Kozyev (R. Pandey and A. N. Kozyev, unpublished) have modified their experimental photodynamic agent, hexylpyropheophorbide (HPPH), with a carotene moiety that suppresses triplet state and renders the therapeutic agent ineffective while preserving its diagnostic fluorescence contrast agent abilities.

Using the same instrumentation and animal model, our group assessed the photodynamic agent HPPH-car. Injected into the canine model, the dye was excited at 660 nm and its fluorescence was collected at 710 nm. With an extinction coefficient of  $45,000 \text{ M}^{-1} \text{ cm}^{-1}$ , a lifetime of 3.6 ns, and quantum efficiency of 0.11, the maximum absorption and emission wavelengths of HPPH-car fall within the melanin and hemoglobin absorbance maxima, making the dye less diagnostically effective [102]. Nonetheless, the pharmacokinetics show HPPH-car to be selectively taken up by an adenocarcinoma of the canine, owing presumably to the dye's association with low-density lipoproteins (LDL) within the plasma and the overexpression of LDL receptors on cancer cells [118]. The use of PDT agents and their modified, non therapeutic forms has long been used for identification of lesions using continuous-wave techniques [119–122]. With the development of newer red-shifted agents, great opportunities exist for employing them as fluorescent diagnostic agents in deep tissues with the potential benefit of added therapeutic action. In addition, because nonmodified PDT agents typically exhibit long fluorescent lifetimes that are dependent on their microenvironment, it is possible to perform nanosecond time-gating following a pulse of light to localize the regions of preferential uptake that usually corresponds to tumor. Cubeddu and coworkers [123] employed this technique by collecting the hematoporphyrin fluorescence after a time delay from an incident impulse of excitation light in a mouse tumor model. Although the tumor depth may have been rather shallow, the work nonetheless represents the first time that fluorescence decay kinetics were employed to induce contrast for imaging and detection.

**4.4.4 Other developments for contrast agents** Several other efforts to design fluorescent NIR contrast agents that target the overexpression of proteases or membrane receptors in pathogenesis have recently appeared in the literature. For example, Tung and colleagues [124] conjugated a cyanine

dye (Cy5.5) onto a peptide with specificity for cathepsin D that is an enzyme common to many neoplasms. Upon conjugation of several dye–peptide dimers to methoxy polyethylene glycol, the fluorescence of the Cy5.5 dyes were quenched due to their close proximity in the complex. However, upon enzymatic cleavage, the dyes were released from the conjugated compound and radiatively re-emitted. The Cy 5.5 dyes tend to also be outside the optimal range for fluorescence near infrared imaging exhibiting an absorbance maximum of 670 and emission maximum at 700 nm. Nonetheless, the group demonstrated the efficacy of their fluorescent agent in cultured cells [124] and millimeter-sized lesions in tumor-bearing mice [125,126]. The excitation/emission of the Cy 5.5 dyes may be suitable for small tissue volume imaging, as in the case of a mouse, but may be restricted from imaging larger tissue volumes as in the case of mammographic imaging.

In earlier work to investigate antibody-targeted delivery of macromolecules in a xenograft model human small cell lung carcinoma, Marecos and coworkers employed green excitable, rhodamine dyes conjugated with the biocompatible graft copolymer and tumor-specific chimeric monoclonal antibodies [127]. Again, to be an effective optical tomographic agent in deep tissues, the dyes must excite and emit in the red range. For example, the ability to image 60- to 800- $\mu\text{m}$ -sized tumor nodules even with green light is afforded by fluorescence in small tissue models such as the mouse. Upon establishing green fluorescent protein expression in human and rodent tumor lines, Yang and coworkers [128] used the green emission to monitor tumor growth and metastases by simply employing a CCD camera to detect the fluorescence generated by CW light. Hence, although promising, these green dyes and green fluorescing proteins are not appropriate for deep tissue imaging such as would be required for diagnostic breast imaging.

In another innovative development, Huber *et al.* [129] synthesized bifunctional contrast agents containing a metal chelator for binding of a paramagnetic ion such as gadolinium, and a conjugated fluorescent dye such as tetramethylrhodamine to combine optical MRI of experimental animals. Although rhodamine excites again within the visible with maximum absorbance at 547 nm and emission at 572 nm, the approach was successful for imaging of *Xenopus laevis* embryos. With the conjugation of an NIR excitable dye, the potential to develop bifunctional contrast agents for deep tissue medical imaging could also be realized. Again the reader should be cautious however in assessing contrast-agent studies conducted in mice and rats. These tissue volumes are not comparable to those in humans and it is unlikely that emission signals at these wavelengths can be detected with sufficient SNR for image reconstruction in large volumes.

## 5.0 Summary, Future Work and Prognosis for NIR Optical Tomography

In summary, we have attempted to provide a concise, yet moderately detailed synopsis of the development of NIR

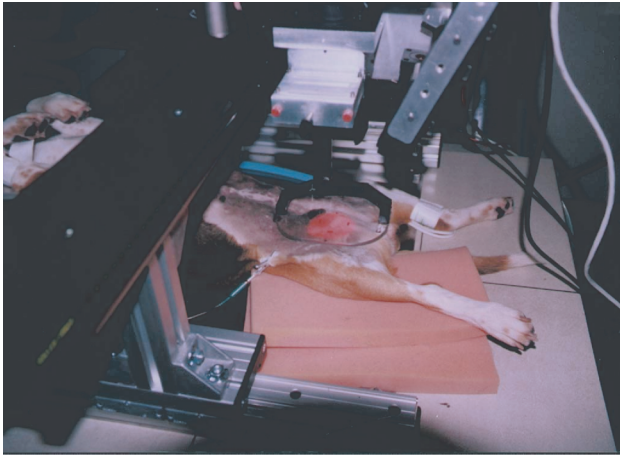


**Figure 18.** Photograph illustrating the use of an incident expanded beam on the mammary chain of the canine to excite systemically administered fluorophore and to collect the emission of generated light from the tissue surface.

optical tomography using CW, TDPM, and FDPM specific for the diagnostic mammography. It is clear from the physics, mathematics, and ultimately the performance of the clinical studies briefly summarized herein, that optical mammography is probably not well suited for screening the general population of women. For optical mammography to be useful as a screening modality, it needs to provide consistent detection of small lesions not already detected by conventional X-ray mammography and preferably in premenopausal women with radiodense breast tissue. Nonetheless, the absorption signatures from NIR techniques can provide information regarding oxygenation status and changes in vascularity owing to anti-angiogenesis agents.

NIR, fluorescent contrast agents offer additional contrast and can, by virtue of their synthesis, impart molecular information to the re-emitted signals detected at the tissue surface. The most immediate opportunity for fluorescence imaging within the human breast is within the sentinel lymph node mapping currently conducted with radionuclides and optical dyes for localization, extraction, and biopsy conducted to provide prognostic indication of the extent of cancer spread. However with further development in “smart” NIR conjugated fluorescent dye complexes that not only target the tissue region of interest, but also “sense” and “turn on” when at the appropriate site involving a specific disease, the ability to perform *in situ* diagnosis with cocktails of molecular imaging agents could be realized. Indeed the fluorescent-dye development in the past 15 years has revolutionized the field of microscopy enabling one to perform molecular imaging in a cellular basis — with the development of suitable NIR dyes of minimal toxicity, the revolution could be translated to enable molecular imaging in whole, living tissues. Although further developments in the measurements, models, and image recovery processes still remain to be accomplished, the

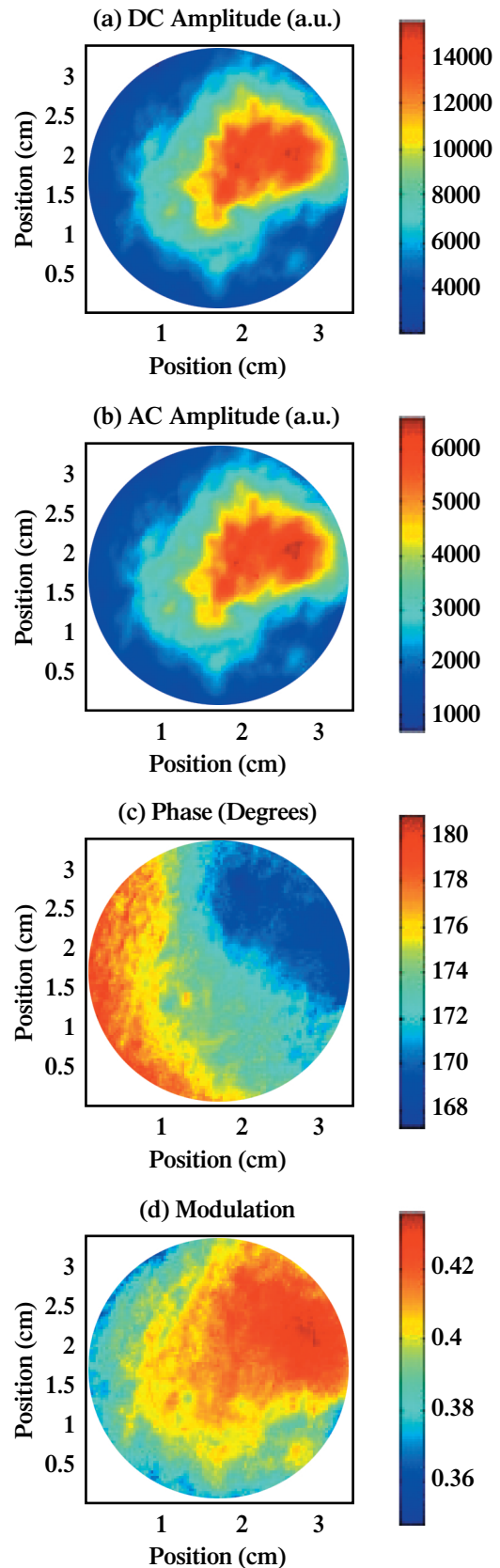


**Figure 19.** The  $128 \times 128$ -pixel-based imaging of 830-nm fluorescence of (a) CW DC, (b) amplitude  $I_{AC}$ , (c) phase delay and (d) modulation ratio of the detected fluorescence generated from the area cranial of the left fourth mammary gland of a canine. Illumination was accomplished with an expanded 780-nm laser diode. Modulation frequency was 100 MHz. Reproduced with permission from Reynolds et al. [104].

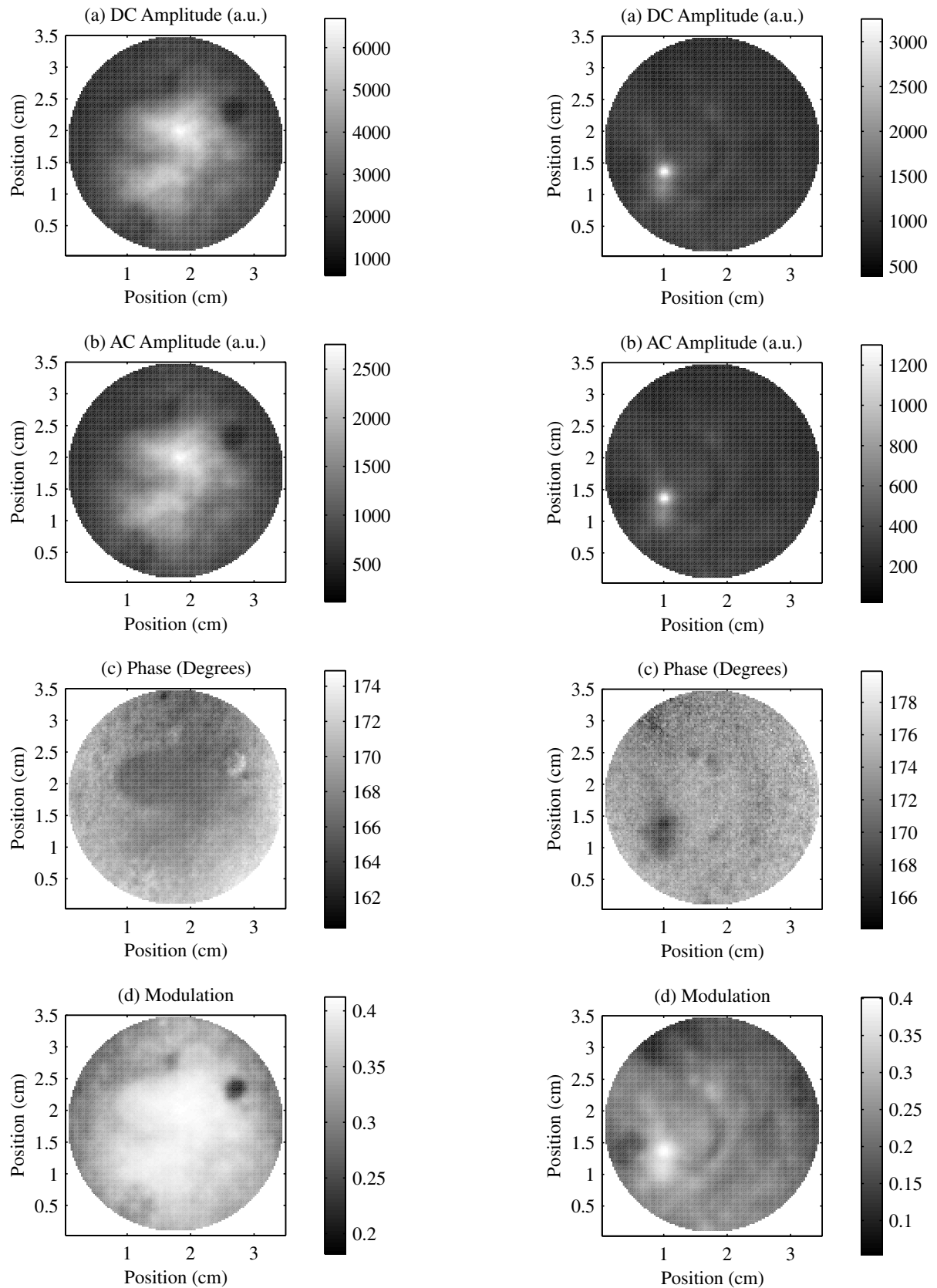


**Figure 20.** The  $128 \times 128$ -pixel-based imaging of 830-nm fluorescence of (a) CW DC, (b) amplitude  $I_{AC}$ , (c) phase delay and (d) modulation ratio of the detected fluorescence generated from the area cranial of the left fifth mammary gland of a canine. Illumination was accomplished with an expanded 780-nm laser diode. Modulation frequency was 100 MHz. Reproduced with permission from Reynolds et al. [104].

**Figure 21.** The  $128 \times 128$ -pixel-based imaging of 830-nm fluorescence of (a) CW DC, (b) amplitude  $I_{AC}$ , (c) phase delay and (d) modulation ratio of the detected fluorescence generated from a lymph node in the area of the right fifth mammary gland. Illumination was accomplished with an expanded 780-nm laser diode. Modulation frequency was 100 MHz. Reproduced with permission from Reynolds et al. [104].

largest challenge remains the sophisticated chemistry of conjugated dyes that excite and emit in the 750- to 850-nm wavelength region.

Breast imaging is an excellent frontier in which to develop fluorescence contrast-enhanced optical tomography owing to the large volume of tissue and the urgent need for diagnostic measures in patients with breast cancer. Although increasing numbers of engineering and medicinal chemistry groups are tackling the subproblems for NIR fluorescence-enhanced contrast imaging identified herein, the clinical applications of agents for diagnostic breast imaging are already emerging [55]. The translation to diagnostic detection of metastases of other cancers may be forthcoming.

### Acknowledgements

The authors acknowledge the contributions from the following present and past members of the Photon Migration Laboratories, which include Anuradha Godavarty, Michael Gurfinkel, Christina L. (Burch) Hutchinson, Eddy Kuwana, Jangwoon Lee, Guadiana Lopez, Ralph Mayer, Dilip Paithankar, Jeffery Reynolds, Ranadhir Roy, Lee Suddeath, Alan Thompson, and Tamara Troy. This assistance of Martha Stafford in the preparation of this manuscript is gratefully acknowledged.

### References

- [1] Tromberg BJ, Shah N, Lanning R, Cerussi A, Espinoza J, Phain T, Svaasand L, and Butler J (2000). Non-invasive *in vivo* characterization of breast tumors using photon migration spectroscopy. *Neoplasia* **2**, 26–40.
- [2] Doornbos RMP, Lang R, Aalders MC, Cross FW, and Sterenborg HJCM (1999). The determination of *in vivo* human tissue optical properties and absolute chromophore concentrations using spatially resolved steady-state diffuse reflectance spectroscopy. *Phys Med Biol* **44**, 967–981.
- [3] Chance B, Leigh JS, Miyake H, Smith DS, Nioka S, Greenfield R, Finander M, Kaufmann K, Levy W, Young M, Cohen P, Yoshioka H, and Boretsky R (1988). Comparison of time-resolved and -unresolved measurements of deoxyhemoglobin in brain. *Proc Natl Acad Sci USA* **85**, 4791–4975.
- [4] Balgi G, Reynolds JS, Mayer RH, Cooley R, and Sevick-Muraca EM (1999). Measurements of multiply scattered light for on-line monitoring of changes in size distribution of cell–debris suspensions. *Biotechnol Prog* **15**, 1106–1114.
- [5] Grosenick D, Wabnitz H, Rinnebert HH, Moesta KT, and Schlag PM (1999). Development of a time-domain optical mammography and first *in vivo* applications. *Appl Opt* **38**, 2927–2943.
- [6] O’Leary MA, Boas DA, Chance B, and Yodh AG (1992). Refraction of diffuse photon density waves. *Phys Rev Lett* **69**, 2658–2661.
- [7] Boas DA, O’Leary MA, Chance B, and Yodh AG (1994). Scattering of diffuse photon density waves by spherical inhomogeneities within turbid media — analytic solutions and applications. *Proc Natl Acad Sci USA* **91**, 4887–4891.
- [8] Schmitt JM, Knüttel A, and Knutson JR (1992). Interference of diffusive light waves. *J Opt Soc Am A* **9**, 1832–1843.
- [9] Chance B, Kang K, He H, and Sevick E (1993). Highly sensitive object location in tissue models with linear in-phase and anti-phase multi-element optical arrays in one and two dimensions. *Proc Natl Acad Sci USA* **90**, 3424–3427.
- [10] Sevick-Muraca EM, Pierce J, Jiang H, and Kao J (1997). Photon migration measurement of latex size distribution in concentrated suspensions. *AIChE J* **43**, 655–664.
- [11] Sevick EM, Chance B, Leigh J, Nioka S, and Maris M (1991). Quantitation of time- and frequency-resolved optical spectra for the determination of tissue oxygenation. *Anal Biochem* **195**, 330–351.
- [12] Ishimaru A (1978). *Wave Propagation and Scattering in Random Media*, Academic Press, New York, NY.
- [13] Case KM, and Zweifel PF (1967). *Linear Transport Theory*, Addison-Wesley, Reading, MA.
- [14] Duderstadt JJ, and Hamilton LJ (1976). *Nuclear Reactor Analysis*, Wiley, New York, NY.
- [15] Patterson MS, Chance B, and Wilson B (1989). Time resolved reflectance and transmittance for the non-invasive measurement of tissue optical properties. *Appl Opt* **28**, 2331–2336.
- [16] Welch AJ, and van Gemert MJC (Eds). (1995). *Optical–Thermal Response of Laser-Irradiated Tissue*, Plenum Welch Press, New York.
- [17] Haskell RC, Svaasand LO, Tsay T-T, Feng T-C, McAdams MS, and Tromberg BJ (1994). Boundary conditions for the diffusion equation in radiative transfer. *J Opt Soc Am A* **11**, 2727–2741.
- [18] Keijzer M, Star WM, and Storch PRM (1988). Optical diffusion in layered media. *Appl Opt* **27**, 1820–1824.
- [19] Hielscher AH, Jacques SL, Wang L, and Tittel FK (1995). The influence of boundary conditions on the accuracy of diffusion theory in time-resolved reflectance spectroscopy of biological tissues. *Phys Med Biol* **40**, 1957–1975.
- [20] Farrell TJ, Patterson MS, and Wilson B (1992). A diffusion theory model of spatially resolved, steady-state diffuse reflectance for the noninvasive determination of tissue optical properties *in vivo*. *Med Phys* **9**, 879–888.
- [21] Roy R, and Sevick-Muraca EM (2000). Three-dimensional unconstrained and constrained image reconstruction techniques applied to fluorescence, frequency-domain photon migration. *Appl Opt* (submitted).
- [22] Jacques SL (1998). Light distributions from point, line, and plane sources for photochemical reactions and fluorescence in turbid biological tissues. *Photochem Photobiol* **67**, 23–32.
- [23] Kim AD, and Ishimaru A (1998). Optical diffusion of continuous-wave, pulsed, and density waves in scattering media and comparisons with radiative transfer. *Appl Opt* **37** (22), 5313–5319.
- [24] Yoo KM, Liu F, and Alfano RR (1990). When does the diffusion approximation fail to describe photon transport in random media? *Phys Rev Lett* **64**, 2647–2649.
- [25] Yao Y, Wang Y, Pei Y, Zhu W, and Barbour RL (1997). Frequency-domain optical imaging of absorption and scattering distributions by a Born iterative method. *J Opt Soc Am A* **14**, 325–342.
- [26] Paithankar DY, Chen AU, Pogue BW, Patterson MS, and Sevick-Muraca EM (1997). Imaging of fluorescent yield and lifetime from multiply scattered light reemitted from random media. *Appl Opt* **36**, 2260–2272.
- [27] Pogue BW, Patterson MS, Jiang H, and Paulsen KD (1995). Initial assessment of a simple system for frequency domain diffuse optical tomography. *Phys Med Biol* **40**, 1709–1729.
- [28] Eppstein MJ, Dougherty DE, Troy TL, and Sevick-Muraca EM (1999). Biomedical optical tomography using dynamic parameterization and Bayesian conditioning on photon migration measurements. *Appl Opt* **38**, 2138–2150.
- [29] Fulton SR, Ciesielski PE, and Schubert WH (1986). Multigrid methods for elliptic problems. A review. *Mon Weather Rev* **114**, 943–959.
- [30] Adams JC (1989). MUDPACK Multigrid portable FORTRAN software for the efficient solution of linear elliptic partial differential equations. *Appl Math Comp* **34**, 113–146.
- [31] Paulsen KD, and Jiang H (1995). Spatially varying optical property reconstruction using a finite element diffusion equation approximation. *Med Phys* **22**, 691–701.
- [32] Schweiger M, Arridge SR, and Delpy DT (1993). Application of the finite element method for the forward and inverse models in optical tomography. *J Math Imag Vision* **3**, 263–283.
- [33] Roy R, and Sevick-Muraca EM (1999). Truncated Newton’s optimization scheme for absorption and fluorescence optical tomography: Part I. Theory and formulation. *Opt Exp* **4**, 353–371.
- [34] Fantini S, Walker SA, Franceschini MA, Kaschke M, Schlag PM, and Moesta KT (1998). Assessment of the size, position, and optical properties of breast tumors *in vivo* by noninvasive methods. *Appl Opt* **37**, 1982–1989.
- [35] Cubeddu R, Pifferi A, Taroni P, and Valentini G (1996). Time-resolved imaging on a realistic tissue phantom:  $\mu_s$  and  $\mu_a$  images versus time-integrated images. *Appl Opt* **35**, 4533–4540.
- [36] Boas DA, O’Leary MA, Chance B, and Yodh AG (1997). Detection and characterization of optical inhomogeneities with diffuse photon density waves: a signal to noise analysis. *Appl Opt* **36**, 75–92.





- [37] Hall DJ, Hebden JC, and Delpy DT (1997). Imaging very low contrast objects in breastlike scattering media with time-resolved method. *Appl Opt* **36**, 7270–7276.
- [38] Barber DC, and Brown BH (1990). Progress in Electrical Impedance Tomography. In *Inverse Problems in Partial Differential Equations*. D Coulton, R Ewing and W Rundell (Eds). Proc. SIAM.
- [39] Matson CL, and Liu H (1999). Backprojection in turbid media. *J Opt Soc Am A* **16**, 1254–1265.
- [40] Colak SB, Papaioannou DG, T'Hooft GW, van der Mark MB, Schomberg H, Paasschens JCJ, Melissen JBM, and van Asten NAAJ (1997). Tomographic image reconstruction from optical projections in light diffusing media. *Appl Opt* **36**, 180–213.
- [41] Grable RJ, Rohler DP, and Kla S (1997). Optical Tomography in Breast Imaging. In *Optical Tomography and Spectroscopy of Tissues: Theory, Instrumentation, Model, and Human Studies*. B Chance and R Alfano (Eds). Proc SPIE, Vol. 2979, Bellingham, WA. p. 197 SPIE, The International Society for Optical Engineering, Bellingham, WA.
- [42] Graber HL, Chang J, Lubowsky J, Aronson R, and Barbour RL (1993). Near infrared absorption imaging of dense scattering media by steady-state diffusion tomography. *Proc SPIE* **1888**, 372–386.
- [43] Walker SA, Fantini S, and Gratton E (1997). Image reconstruction by backprojection from frequency-domain optical measurements in highly scattering media. *Appl Opt* **36**, 180–213.
- [44] Van der Mark MB, T'Hooft GW, Wachters AJH, de Vries UH, Janseen JP, and Wasser MNJN (2000). *Clinical Study of the Female Breast Using Spectroscopic Diffuse Optical Tomography*. Proceedings of the OSA Topical Biomedical Optics Meeting, Miami Beach, April 2–5. The Optical Society of America, Washington, D.C., pp. 514–518.
- [45] Cheney M (1990). A Review of Multidimensional Inverse Potential Scattering. In *Inverse Problems in Partial Differential Equations*. D Colton, R Ewing and W Rundell (Eds). Proc. SIAM. SIAM Press, Philadelphia, PA, pp. 37–49.
- [46] O'Leary MA, Boas D, Chance B, and AG Yodh (1995). Experimental images of heterogeneous turbid media by frequency-domain diffusing photon tomography. *Opt Lett* **20**, 426–428.
- [47] Gonatas CP, Ishii M, Leigh JS, and Shotland JC (1995). Optical diffusion imaging using a direct inversion method. *Phys Rev E* **52**, 4361–4365.
- [48] Cheng X, and Boas DA (1998). Diffuse optical reflection tomography with continuous-wave illumination. *Opt Exp* **3**, 118–123.
- [49] Sevick-Muraca EM, Heintzelman DL, Lee J, Troy TL, and Paithankar DY (1997). The role of higher order scattering in solutions to the forward and inverse optical imaging problems in random media. *Appl Opt* **36**, 9058–9067.
- [50] Chew CW, and Wang YM (1990). Reconstruction of two-dimensional permittivity distribution using the distorted Born iterative method. *IEEE Trans Med Imaging* **9**, 218–225.
- [51] Ye JC, Webb KJ, Millane RP, and Downar TJ (1999). Modified distorted Born iterative method with an approximate Frechet derivative for optical diffusion tomography. *J Opt Soc Am A* **16**, 1814–1826.
- [52] Arridge SR (1999). Optical tomography in medical imaging. *Inverse Probl* **15**, R41–R93.
- [53] Pogue BW, McBride TO, Prewitt J, Osterberg UL, and Paulsen KD (1999). Spatially variant regularization improves diffuse tomography. *Appl Opt* **38**, 2950–2961.
- [54] Hielscher AH, Klose AD, and Manson KM (1999). Gradient-based iterative image reconstruction scheme for time-resolved optical tomography. *IEEE Trans Med Imaging* **18**, 262–271.
- [55] Ntziachristos V, Yodh AG, Schnall M, and Chance B (2000). Concurrent MRI and diffuse optical tomography of the breast after indocyanine green enhancement. *Proc Natl Acad Sci USA* **97**, 2767–2772.
- [56] Pei Y, Lin F-B, and Barbour RL (1999). Modeling of sensitivity and resolution to an included object in homogeneous scattering media and in MRI-derived breast maps. *J Biomed Opt* **5**, 302–219.
- [57] Pogue BW, and Paulsen KD (1998). High-resolution near-infrared tomographic imaging simulations of the rat cranium by use of a priori magnetic resonance imaging structural information. *Opt Lett* **23**, 1716–1718.
- [58] Holboke MJ, Tromberg BJ, Li X, Shah N, Fishkin J, Kidney D, Butler J, Chance B, and Yodh AG (2000). Three-dimensional diffuse optical mammography with ultrasound localization in a human subject. *J Biomed Opt* **5**, 237–247.
- [59] Schmidt FEW, Hebden JC, Hillman NC, Fry ME, Schweiger M, Dehghani H, Delpy DT, and Arridge SR (2000). Multi-slice imaging of a tissue equivalent phantom by use of time resolved optical tomography. *Appl Opt* **39**, 3380–3387.
- [60] Arridge SR, Hebden JC, Schweiger M, Schmidt FEW, Fry ME, Hillman EMC, Dehghani H, and Delpy DT (2000). A method for three-dimensional time-resolved optical tomography. *Int J Imaging Syst Technol* **2**, 2–11.
- [61] Jiang H, Xu Y, Iftimia N (2000). Experimental three-dimensional optical image reconstruction of heterogeneous turbid media from continuous-wave data. *Opt Express* **7**, 204–209.
- [62] Eppstein MJ, Dougherty DE, Hawrysz DJ, and Sevick-Muraca EM (2000). Three-Dimensional Fluorescence Absorption Imaging With Domain Decomposition. In *Biomedical Topical Meetings. OSA Technical Digest*. Optical Society of America, Washington, DC. pp. 173–175.
- [63] Cutler M (1929). Transillumination as an aid in the diagnosis of breast lesions. *Surg Gynecol Obstet* **6**, 721–729.
- [64] Colak SB, van der Mark MB, Hooft GW, Hoogenraad JH, van der Linden ES, and Kuipers FA (1999). Clinical optical tomography and NIR spectroscopy for breast cancer detection. *IEEE J Sel Top Quantum Electron* **5**, 1143–1158.
- [65] Grable R, Gkanatis NA, and Ponder SL (2000) Optical mammography. *Appl Radiol*, February 29, 18–20.
- [66] Grosenick D, Wabnitz H, and Rinneberg H (1997). Time resolved imaging of solid phantoms for optical mammography. *Appl Opt* **36**, 221–231.
- [67] Cubeddu R, Pifferi A, Taroni P, Torricelli A, and Valentini G (1999). Noninvasive absorption and scattering spectroscopy of bulk diffusive media: an application to the optical characterization of human breast. *Appl Phys Lett* **74**, 874–876.
- [68] Franceschini MA, Moesta KT, Fantini S, Gaida G, Gratton E, Jess H, Mantulin WW, Seeber M, Schlag PM, and Kaschke M (1997). Frequency-domain techniques enhance optical mammography: initial clinical results. *Proc Natl Acad Sci USA* **94**, 6468–6473.
- [69] Moesta K, Fantini S, Jess H, Totkas S, Franceschini M, Kaschke M, and Schlag P (1998). Contrast features of breast cancer in frequency-domain laser scanning mammography. *J Biomed Opt* **3**, 129–136.
- [70] McBride TO, Pogue B, Gerety ED, Poplack SB, Osterberg UL, and Paulsen KD (1999). Spectroscopic diffuse optical tomography for the quantitative assessment of hemoglobin and oxygen saturation in breast tissue. *Appl Opt* **38**, 5480–5490.
- [71] Sevick-Muraca EM, and Paithankar DY. Fluorescence imaging system and measurement. U.S. patent #5,865,754, issued 2/2/99.
- [72] Paithankar DY, Chen A, and Sevick-Muraca EM (1996). Fluorescence Yield and Lifetime Imaging in Tissues and Other Scattering Media. In *Laser and Light Spectroscopy to Diagnose Cancer and Other Diseases III: Optical Biopsy*. RR Alfano (Ed). Proc. Soc. Photo-Opt. Instrum. Eng., Vol. 2679, pp. 162–175.
- [73] Lakowicz JR (1983). *Principles of Fluorescence Spectroscopy*. Plenum, New York.
- [74] Mordon S, Devoisselle JM, and Maunoury V (1994). *In vivo* pH measurement and imaging of a pH-sensitive fluorescent probe (5-6 carboxyfluorescein): instrumental and experimental studies. *Photochem Photobiol* **60**, 274–279.
- [75] Russell DA, Pottier RH, and Valenzano DP (1994). Continuous noninvasive measurement of *in vivo* pH in conscious mice. *Photochem Photobiol* **59**, 309–313.
- [76] Vinogradov SA, Lo LW, Jenkins WT, Evans SM, Koch C, and Wilson DF (1996). Non-invasive imaging of the distribution of oxygen tension in tissue *in vivo* using near infrared phosphors. *Biophys J* **70**, 1209–1617.
- [77] Sevick-Muraca EM, Lopez G, Troy TL, Reynolds JS, and Hutchinson CL (1997). Fluorescence and absorption contrast mechanisms for biomedical optical imaging using frequency-domain techniques. *Photochem Photobiol* **66**, 55–64.
- [78] Li X, Chance B, and Yodh AG (1998). Fluorescence heterogeneities in turbid media, limits for detection, characterization, and comparison with absorption. *Appl Opt* **37**, 6833–6843.
- [79] Zhu XD, Wei S-P, and Guo XW (1997). Imaging objects in tissue-like media with optical tagging and the diffuse photon differential transmittance. *J Opt Soc Am* **14**, 300–305.
- [80] Sevick-Muraca EM, and Burch CL (1994). Origin of phosphorescence re-emitted from tissues. *Opt Lett* **19**, 1928–1930.
- [81] Richards-Kortum R, and Sevick-Muraca EM (1996). Quantitative optical spectroscopy for tissue diagnostics. *Annu Rev Phys Chem* **47**, 555–606.
- [82] Kuwana E (2000). Measurement and model assessment of fluorescence multi-exponential decay kinetics and propagation in scattering media. MS thesis chemical engineering, Purdue University.



- [83] Chennomordik V, Hattery D, Gannot I, and Gandjbakhche AH (1999). Inverse method 3-D reconstruction of localized *in vivo* fluorescence — application to Sjogren syndrome. *IEEE J Sel Top Quantum Electron* **54**, 930–935.
- [84] Hattery D, Chennomordik V, Gannot I, Loew M, and Gandjbakhche AH (2000). Fluorescence measurement of localized, deeply embedded physiological processes. *Proc SPIE* **3978**, 377–382.
- [85] Patterson MS, and Pogue BW (1994). Mathematical model for time-resolved and frequency-domain fluorescence spectroscopy in biological tissue. *Appl Opt* **33**, 1963–1964.
- [86] Hutchinson CL, Lakowicz JR, and Sevick-Muraca EM (1995). Fluorescence lifetime-based sensing in tissues: a computational study. *Biophys J* **68**, 1574–1582.
- [87] Fantini S, and Gratton E (2000). Fluorescence photon density waves in optically diffuse media. *Optic Commun* **173**, 73–79.
- [88] Mayer RH, Reynolds JS, and Sevick-Muraca EM (1999). Measurement of fluorescence lifetime in scattering media using frequency-domain photon migration. *Appl Opt* **38**, 4930–4938.
- [89] Cerussi AE, Maier JS, Fantini S, Franceschini MA, Mantulin WW, and Gratton E (1997). Experimental verification of a theory for time-resolved fluorescence spectroscopy of thick tissues. *Appl Opt* **36**, 116–124.
- [90] Wu J, Wang Y, Perleman L, Itzkan I, Dasari RR, and Feld MS (1995). Time-resolved multichannel imaging of fluorescent objects embedded in turbid media. *Opt Lett* **20**, 489–491.
- [91] Hull EL, Nichols MG, and Foster TH (1998). Localization of luminescent inhomogeneities in turbid media with spatially resolved measurements of cw diffuse luminescence emittance. *Appl Opt* **37**, 2755–2765.
- [92] Schotland JC (1997). Continuous-wave diffusion imaging. *J Opt Soc Am A* **14**, 275–279.
- [93] Chang J, Graber HL, and Barbour RL (1997). Imaging of fluorescence in highly scattering media. *IEEE Trans Biomed Eng* **44**, 810–822.
- [94] Chang J, Graber HL, and Barbour RL (1998). Improved reconstruction algorithm for luminescence when background luminophore is present. *Appl Opt* **37**, 3547–3552.
- [95] O'Leary MA, Boas DA, Li XD, Chance B, and Yodh AG (1996). Fluorescence lifetime imaging in turbid media. *Opt Lett* **21**, 158–160.
- [96] Lee J, and Sevick-Muraca EM. Fluorescence enhanced absorption imaging: noise tolerance characteristics compared with conventional absorption and scattering imaging. *J Biomed Opt*. In press.
- [97] Eppstein MJ, Dougherty DE, Hawrysz DJ, and Sevick-Muraca EM (2000). 3-D Bayesian optical imaging reconstruction with domain decomposition. Submitted January 2000. *IEEE Trans. Med. Imag*. In press.
- [98] Hawrysz DJ, Eppstein MJ, and Sevick-Muraca EM (2000). Measurement and model error assessment of a single pixel, frequency-domain photon migration apparatus and diffusion model for imaging applications. *Proc SPIE* **4160**.
- [99] Lyubimov (2000). Principles of fluorescence laser tomography of strongly scattering media. *Phys Quantum Opt* **88**, 321–324.
- [100] Landsman ML, Kwant G, Mook G, and Zijlstra WG (1976). Light-absorbing properties, stability, and spectral stabilization of Indocyanine green. *J Appl Physiol* **40**, 575–583.
- [101] Mordon S, Devoisselle JM, Soulie-Begu S, and Desmettre T (1998). Indocyanine green: physiochemical factors affecting its fluorescence *in vivo*. *Microvasc Res* **55**, 146–152.
- [102] Gurfinkel M, Thompson AB, Ralston W, Troy TL, Moore AL, Moore TA, Gust JD, Tatman D, Reynolds JS, Muggenburg B, Nikula K, Pandey R, Mayer RH, Hawrysz DJ, and Sevick-Muraca EM (2000). Pharmacokinetics of ICG and HPPH-car for the detection of normal and tumor tissue using fluorescence, near-infrared reflectance imaging: a case study. *Photochem Photobiol* **72**, 94–102.
- [103] Reynolds JS, Troy TL, and Sevick-Muraca EM (1997). Multi-pixel techniques for frequency-domain photon migration imaging. *Biotechnol Prog* **13**, 669–680.
- [104] Reynolds JS, Troy TL, Mayer R, Thompson AB, Waters DJ, Cornell KK, Snyder PW, and Sevick-Muraca EM (1999). Imaging of spontaneous canine mammary tumors using fluorescent contrast agents. *Photochem Photobiol* **70**, 87–94.
- [105] Schafer KA, Kelly JF, Schrader R, Griffith WC, Muggenburg BA, Tierney LA, Lechner GF, Janovitz EB, and Hahn FF (1998). A canine model of familial mammary gland neoplasia. *Vet Pathol* **35**, 168–177.
- [106] Lakowicz J, and Berndt K (1991). Lifetime-sensitive fluorescence imaging using an rf phase-camera. *Rev Sci Instrum* **62**, 1727–1734.
- [107] Sevick EM, Lakowicz JR, Szmajcinski H, Nowaczyk K, and Johnson M (1992). Frequency-domain imaging of obscure absorbers: principles and applications. *J Photochem Photobiol* **16**, 169–185.
- [108] Moore MP, and Kinne DW (1998). The surgical management of primary invasive breast cancer. *Ca-Cancer J Clin* **45**, 000–000.
- [109] McMaster KM, Giuliano AE, Ross MI, Reintgen DS, Hunt KK, Klimberg VS, Whitworth PW, Tafta LC, and Edwards MJ (1998). Sentinel lymph node biopsy for breast cancer — not yet the standard of care. *N Engl J Med* **339**, 990–995.
- [110] Krag D, Weaver D, Ashikaga T, Moffat F, Klimberg S, Shriver C, Feldman S, Kusminsky R, Gadd M, Kuhn J, Harlow S, Beitsch P, Whitworth P, Foster R Jr, and Dowlatsahi K (1998). The sentinel node in breast cancer — a multicenter validation study. *N Engl J Med* **339**, 941–946.
- [111] Ntziachristos V, Ma X, and Chance B (1998). Time-correlated single photon counting imager for simultaneous magnetic resonance and near-infrared mammography. *Rev Sci Instrum* **69**, 4221–4233.
- [112] Maguruma N, Ito S, Bando T, Taoka S, Kusaka Y, Hayashi S, Ichikawa S, Matsunaga Y, Tada Y, Okamura S, Ii K, Imaizumi K, Nakamura K, Takessako K, and Shibamura S (1999). Labeled carcinoembryonic antigen antibodies excitable by infrared rays: a novel diagnostic method for microcancers in the digestive tracts. *Intern Med* **38**, 537–742.
- [113] Sakanti K, Kashiwasake-Jibu M, Taka Y, Wang SM, Zuo H, Yamamoto K, and Shimizu K (1997). Non-invasive optical imaging of the subarachnoid space and cerebrospinal fluid pathways based on near-infrared fluorescence. *J Neurosurg* **87**, 738–745.
- [114] Becker A, Licha K, Kresse M, Riefke BM, Sukiwski U, Ebert B, Rinneberg H, and Semmler W (1999). Transferrin-mediated tumor delivery of contrast media for optical imaging and magnetic resonance imaging. *Proc SPIE* **2600**, 142–150.
- [115] Becker A, Riefke B, Bernd E, Suowski U, Rinnebert H, Semmler W, and Licha K (2000). Macromolecular contrast agents for optical imaging of tumors: comparison of indotricarbocyanine-labeled human serum albumin and transferrin. *Photochem Photobiol* **72**, 234–241.
- [116] Licha K, and Becker A (1999). New contrast agents for optical imaging: acid cleavable conjugates of cyanine dyes with biomolecules. *Proc SPIE* **3600**, 29–35.
- [117] Achilefu S, Dorchow RB, Bigaj JE, and Rajogopalan R (2000). Novel receptor-targeted fluorescent contrast agents for *in vivo* tumor imaging. *Invest Radiol* **35**, 479–485.
- [118] Hasan T, and Parrish JA (1997). Photodynamic Therapy of Cancer. In *Cancer Medicine*. Vol. 1 (4th ed). JF Holland, E Frei, RC Bast, DW Kufe, DL Morton and RR Weichselbaum (Eds). Williams and Wilkins, Philadelphia. pp. 739–751.
- [119] Reddi E, Segalla A, Jori G, Kerrigan PK, Lidell PA, Moore AL, Moore TA, and Gust D (1994). Carotenoporphyrins as selective photo-diagnostic agents for tumors. *Br J Cancer* **69**, 40–45.
- [120] Takemura T, Nakajima S, and Sakata I (1994). Tumor-localizing fluorescent diagnostic agents without phototoxicity. *Photochem Photobiol* **59**, 366–370.
- [121] Rokahr I, Andersson-Engels S, Svanberg S, D'Hallewin M, Baert L, Wang I, and Svanberg K (1995). Optical detection of human urinary bladder carcinoma utilizing tissue autofluorescence and protoporphyrin IX-induced fluorescence following low dose ALA. *Proc SPIE* **2627**, 2–12.
- [122] Nilsson AM, von Holstein CS, Andersson-Engels S, Willen R, Walther B, and Svanberg K (1995). Clinical detection studies of Barrett's metaplasia and oesophageal adenocarcinoma by means of laser-induced fluorescence. *Proc SPIE* **2627**, 49–56.
- [123] Cubeddu R, Canti G, Pifferi A, Taroni P, and Valentini G (1997). Fluorescence lifetime imaging of experimental tumors in hematoporphyrin derivative-sensitized mice. *Photochem Photobiol* **66**, 229–236.
- [124] Tung CH, Bredow S, Mahmood U, and Weissleder R (1999). Preparation of a cathepsin D sensitive near-infrared fluorescent probe for imaging. *Bioconjugate Chem* **10**, 893–896.
- [125] Mahmood U, Tung C-HA, and Weissleder R (1999). Near-infrared optical imaging of protease activity for tumor detection. *Radiology* **214**, 866–870.
- [126] Weissleder R, Tung CH, Mahmood U, and Bogdanov A (1999). *In vivo* imaging of tumors with protease-activated near-infrared fluorescent probes. *Nat Biotechnol* **4**, 375–378.
- [127] Marecos E, Weissleder R, and Bogdanov A (1998). Anti-body mediated versus nontargeted delivery in human small cell lung carcinoma. *Bioconjugate Chem* **9**, 184–191.



- [128] Yang M, Baranov E, Jiang P, Sun FX, Li XM, Li LN, Hasegawa S, Bouvet M, Al-Tuwaijri M, Chishima T, Shimada H, Moossa AR, Penman S, and Hoffman RM (2000). Whole body, optical imaging of green fluorescent protein-expressing tumors and metastases. *Proc Natl Acad Sci USA* **97**, 1206–1211.
- [129] Huber MM, Staubili AB, Kustedjo K, Gray MHB, Shih J, Fraser S, Jacobs RE, and Meade TJ (1998). Fluorescently detectable magnetic resonance imaging agents. *Bioconjugate Chem* **9**, 242–249.
- [130] Tromberg BJ, Coquoz O, Fishkin JB, Pham T, Anderson ER, Bulter J, Cahn M, Gross JD, Venugopalan V, and Plam (1997). Non-invasive measurements of breast tissue optical properties using frequency-domain photon migration. *Philos Trans R Soc London B* **352**, 661–668.
- [131] Heusmann H, Koelzer JG, and Mitic G (1996). Characterization of female breasts *in vivo* by time-resolved and spectroscopic measurements in near infrared spectroscopy. *J Biomed Opt* **1**, 425–434.
- [132] Peters VG, Wyman DR, Patterson MS, and Frank GL (1990). Optical properties of normal and diseased human breast tissues in the visible and near infrared. *Phys Med Biol* **35**, 1317–1334.
- [133] Troy TL, Page DL, and Sevick-Muraca EM (1996). Optical properties of normal and diseased breast tissues: prognosis for optical mammography. *J Biomed Opt* **1**, 342–355.
- [134] Suzuki K, Yamashita Y, Ohta K, and Chance B (1994). Quantitative measurement of optical parameters in the breast using time-resolved spectroscopy. *Invest Radiol* **29**, 410–414.
- [135] Cheong WF, Prahl SA, and Welch AJ (1990). A review of the optical properties of biological tissues. *IEEE J Quant Electron* **26**, 2166–2185.
- [136] Beek JF, Blokland P, Posthumus P, Aalders M, Pickering JW, Sterenberg HJCM, and van Germert MJC (1997). *In vitro* double-integrating-sphere optical properties of tissues between 630 and 1064 nm. *Phys Med Biol* **42**, 2255–2261.
- [137] Fishkin JB, Coquoz O, Anderson ER, Brenner M, and Tromberg BJ (1997). Frequency-domain photon migration measurements of normal and malignant tissue optical properties in a human subject. *Appl Opt* **36**, 10–20.
- [138] Pogue BW, Patterson MS, and Farrell TJ (1995). Forward and inverse calculations for 3D frequency-domain diffuse optical tomography. *Proc SPIE* **2389**, 328–339.
- [139] Jiang H, Paulsen KD, Osterberg UL, Pogue BW, and Patterson MS (1996). Optical image reconstruction using frequency-domain data: simulations and experiments. *J Opt Soc Am A* **13**, 253–266.
- [140] Schweiger M, and Arridge SR (1998). Comparison of two- and three-dimensional reconstruction methods in optical tomography. *Appl Opt* **37**, 7419–7428.
- [141] Gao F, Niu H, Zhao H, and Zhang H (1998). The forward and inverse models in time-resolved optical tomography imaging and their finite-element solutions. *Image Vision Comput* **16**, 703–712.
- [142] O'Leary MA, Boas DA, Chance B, and Yodh AG (1994). Reradiation and imaging of diffuse photon density waves using fluorescent inhomogeneities. *J Lumin* **60, 61**, 281–286.
- [143] Eppstein MJ, Dougherty DE, Hawrysz DJ, and Sevick-Muraca EM (1999). Three-dimensional optical tomography. *Proc SPIE* **3597**, 97–105.